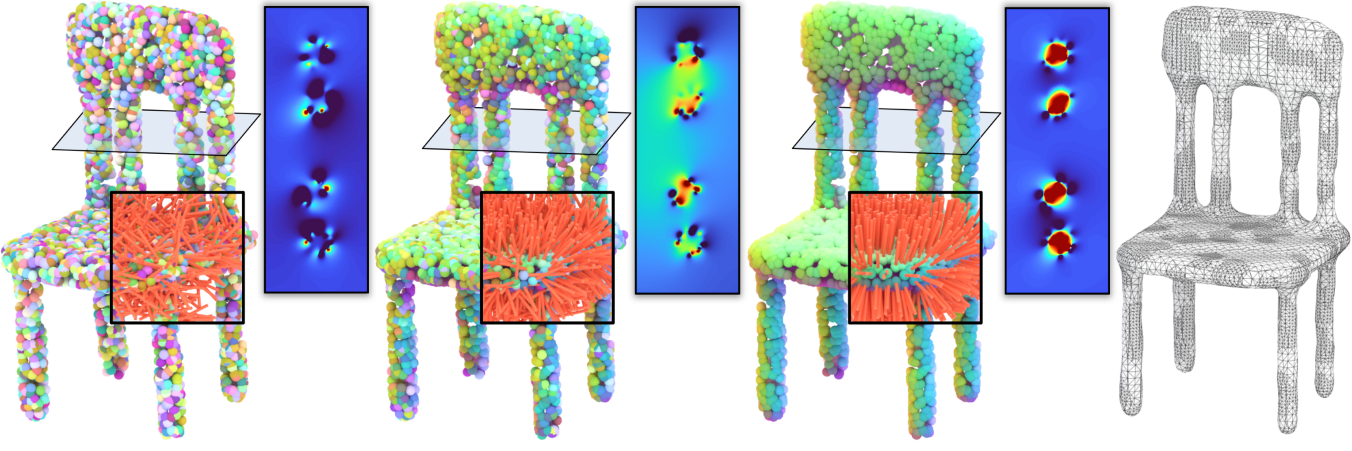
Globally Consistent Normal Orientation for Point Clouds by Regularizing the Winding-Number Field

RUI XU, Shandong University, China
ZHIYANG DOU, The University of Hong Kong, China
NINGNA WANG, The University of Texas at Dallas, USA
SHIQING XIN*, Shandong University, China
SHUANGMIN CHEN, Qingdao University of Science and Technology, China
MINGYAN JIANG, Shandong University, China

XIAOHU GUO, The University of Texas at Dallas, USA

WENPING WANG, Texas A&M University, USA

CHANGHE TU*, Shandong University, China



(a) Initial normal vectors

(b) 20 iterations

(c) 40 iterations

(d) Reconstruction

Fig. 1. For a closed and orientable surface, the winding number is 0 on the exterior and 1 on the interior. Inspired by this fact, in this paper we consider a reverse problem: given an un-oriented point cloud, is it possible to find the globally consistent normal orientations by regularizing the winding-number distribution? We propose a smooth objective function to characterize the requirements of an acceptable winding-number field. Starting from a set of completely random normals (a), we repeatedly optimize their directions (b,c) until the objective function cannot be reduced. With the computed normals, one can simply call the screened Poisson reconstruction (SPR) solver to produce the final surface (d). Note that we use RGB mapping to visualize the normals and provide a sectional view to visualize the change of the winding-number field, where "blue" and "red" indicate 0 and 1, respectively.

Estimating normals with globally consistent orientations for a raw point cloud has many downstream geometry processing applications. Despite tremendous efforts in the past decades, it remains challenging to deal with an unoriented point cloud with various imperfections, particularly in the presence of data sparsity coupled with nearby gaps or thin-walled structures. In this paper, we propose a smooth objective function to characterize the requirements of an acceptable winding-number field, which allows one to find the globally consistent normal orientations starting from a set of completely random normals. By taking the vertices of the Voronoi diagram of the point cloud as examination points, we consider the following three requirements:

Authors' addresses: Rui Xu, Shandong University, China, xrvitd@163.com; Zhiyang Dou, The University of Hong Kong, China, zhiyang0@connect.hku.hk; Ningna Wang, The University of Texas at Dallas, USA, ningna.wang@utdallas.edu; Shiqing Xin, Shandong University, China, xinshiqing@sdu.edu.cn; Shuangmin Chen, Qingdao University of Science and Technology, China, csmqq@163.com; Mingyan Jiang, Shandong University, China, jiangmingyan@sdu.edu.cn; Xiaohu Guo, The University of Texas at Dallas, USA, xguo@utdallas.edu; Wenping Wang, Texas A&M University, USA, wenping@tamu.edu; Changhe Tu, Shandong University, China, chtu@sdu.edu.cn.

(1) the winding number is either 0 or 1, (2) the occurrences of 1 and the occurrences of 0 are balanced around the point cloud, and (3) the normals align with the outside Voronoi poles as much as possible. Extensive experimental results show that our method outperforms the existing approaches, especially in handling sparse and noisy point clouds, as well as shapes with complex geometry/topology.

CCS Concepts: • Computing methodologies \rightarrow Point-based models.

Additional Key Words and Phrases: raw point cloud, normal orientation, winding number, Voronoi diagram, optimization

1 INTRODUCTION

An unoriented point cloud becomes more informative if it is equipped with a set of normals with globally consistent orientations. Predicting reliable normals serves as a crucial step for many downstream tasks, e.g., surface reconstruction [Kazhdan 2005; Kazhdan et al. 2006; Kazhdan and Hoppe 2013; Wang et al. 2021; Xu et al.

 $^{^{\}star}\text{Co-corresponding}$ authors: Shiqing Xin and Changhe Tu.

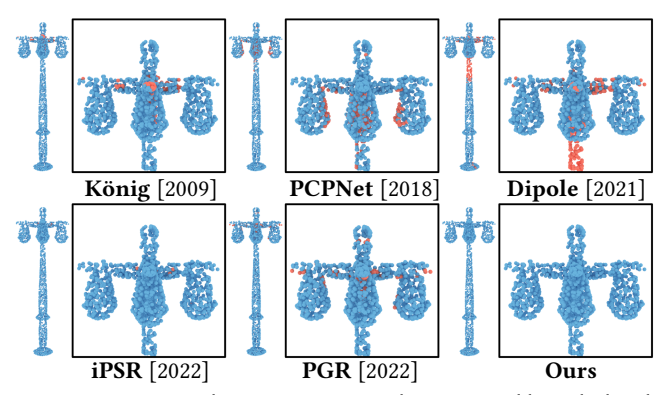


Fig. 2. Existing normal orientation approaches are not able to deal with various imperfections such as noise, thin structures, nearby surfaces and sharp features. Note that the red points indicate a false orientation, *i.e.*, the angle between the ground-truth normal and the predicted normal is larger than 90 degrees.

2022], shape registration [Pomerleau et al. 2015], determining inside/outside information [Barill et al. 2018; Jacobson et al. 2013], shape analysis [Dou et al. 2022; Grilli et al. 2017; Zapata-Impata et al. 2019]. Despite significant progress [Alliez et al. 2007; Boltcheva and Lévy 2017; Dey and Goswami 2004; Dey et al. 2005; Guerrero et al. 2018; Hoppe et al. 1992; Hou et al. 2022; König and Gumhold 2009; Li et al. 2022; Mérigot et al. 2010; Metzer et al. 2021] being made on this problem, it is still a stumbling task of discovering the globally consistent normals for an unoriented point cloud while allowing for various imperfections.

Most of the existing research works [Alliez et al. 2007; Cazals and Pouget 2005; Hoppe et al. 1992; Levin 1998; Pauly et al. 2003] first compute a normal tensor for each point, regardless of orientation, followed by spreading the orientation flags through propagation [Metzer et al. 2021]. They are not able to deal with various imperfections such as noise, thin structures, nearby surfaces, and sharp features since the normals do not rigorously satisfy the property of spatial coherence. In contrast, the recently proposed iPSR [Hou et al. 2022] and Parametric Gauss Reconstruction (PGR) [Lin et al. 2022] focus more on the global consistency of normal orientations, and achieve better results. However, they still suffer from data sparsity coupled with nearby gaps, thin-walled structures, or highly complex geometry/topology. Fig. 2 demonstrates the results of various approaches, where the red points indicate a false orientation.

In recent years, the winding number, as a powerful tool for insideoutside tests, has gained increasing attention in digital geometry processing, ranging from meshing [Hu et al. 2018] to reconstruction [Barill et al. 2018; Wang et al. 2022b]. Despite the ability to distinguish the interior part (the winding number is close to 1) from the exterior part (the winding number is close to 0), it heavily depends on the support of reliable normals. Our hypothesis is that only when the normals are oriented with global consistency, the winding-number field could be approximately binary-valued with 1 and 0. This inspires us to optimize the normals such that the winding-number field becomes fully regularized. Based on this hypothesis, we propose an all-in-one functionality to characterize the requirements of a winding-number field from three aspects: (a) the winding number should be close to either 1 or 0 at any query point, (b) when the query points are scattered in the neighborhood of input samples \mathbf{p}_i , the occurrences of 1 and the occurrences of 0 should be approximately balanced, and (c) the sample \mathbf{p}_i 's normal vector should align well with the direction towards the outside Voronoi pole [Amenta and Bern 1998]. Note that the first two requirements are used to regularize the distribution of the winding number while the last requirement enforces the computed normals to be as accurate as the Voronoi-based approaches [Alliez et al. 2007]. The three terms can be integrated into a smooth objective function with regard to the normals such that the best configuration of normals can be found by solving an unconstrained optimization.

In the implementation, we use L-BFGS to solve the proposed optimization problem. Starting from a completely random normal setting, it generally requires about 30-50 iterations to arrive at the termination. We use the same set of parameters to test our method on various unoriented point clouds, including synthetic data and real scans. Both quantitative statistics and visual comparison show that our method has the advantage of normal accuracy and consistency. It is not only robust to noise and data sparsity (see Fig. 12 and Fig. 14), but also can handle challenging shapes with complex geometry/topology (see Fig. 19). Furthermore, our method can be even applied to incomplete point clouds that encode an open surface (see Fig. 17). In Fig. 3, we provide a gallery of results produced by our approach.

2 RELATED WORK

2.1 Estimating Normal Orientations for Point Clouds

The problem of point cloud orientation has been extensively researched in the past decades. In general, attention must be paid to orientation and accuracy for achieving normal consistency. Existing methods can be divided into two categories: optimization methods and learning techniques. The latter can be further divided into regression-based approaches and surface fitting-based approaches.

Optimization-based Approaches. Hoppe et al. [1992] pioneered on normal orientation. Their approach first uses Principal Component Analysis (PCA) to initialize the normal tensors, and then makes their orientations consistent by a minimum spanning tree (MST) based propagation. Besides the MST-based propagation, more propagation strategies include multi-seed [Xie et al. 2004], Hermite curve [König and Gumhold 2009], and edge collapse [Jakob et al. 2019]. The dipole propagation [Metzer et al. 2021] is also a competing algorithm for propagating the orientation flags. In terms of accuracy improvement, many techniques are proposed, e.g., exponentially decaying function [Levin 2004], local least square fitting [Mitra and Nguyen 2003], truncated Taylor expansion [Cazals and Pouget 2005], moving least squares [Levin 1998], multi-scale kernel [Aroudj et al. 2017], ensemble framework [Yoon et al. 2007]. Wang et al. [2012] proposed to minimize a combination of the Dirichlet energy and the coupledorthogonality deviation such that the normals are perpendicular to the surface of the underlying shape. In terms of handling sparse data, VIPSS [Huang et al. 2019], as a variational method, reconstructs an implicit surface from an un-oriented point set.

There are also many research works on orienting normal vectors for shapes with corners or geometry edges. For example, L0 norm [Sun et al. 2015] or L1 norm [Avron et al. 2010; Sun et al.

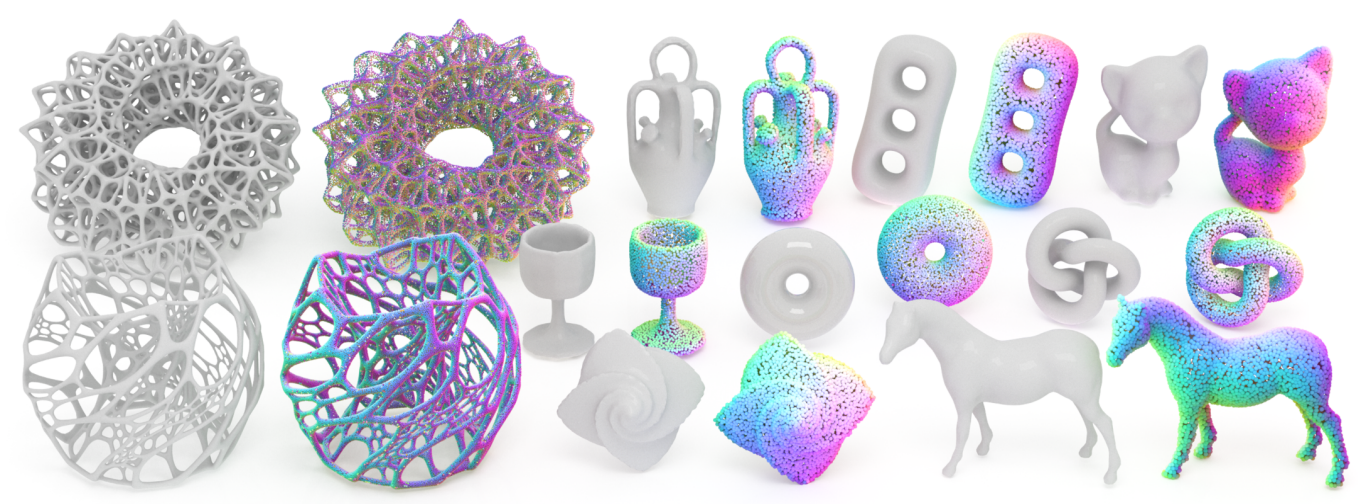


Fig. 3. We equip the input unoriented point clouds with our computed normals (rendered with RGB mapping). By feeding the points and the normals together into the screened Poisson reconstruction (SPR) solver, we get high-fidelity reconstruction results (in gray), which exhibit the high quality of the computed normals.

2015] is based on the observation that a general surface is smooth almost everywhere except at some small number of sharp features. As each feature point is allowed to own a range of normal vectors, Zhang et al. [2018] employed the pair consistency voting strategy to compute multiple normals for feature points. Xu et al. [2022] used optimal transport to regularize normal vectors for the points nearby geometry edges. Besides, statistics and subspace segmentation [Li et al. 2010; Liu et al. 2015; Zhang et al. 2013] are used to estimate normals for point clouds with sharp features.

In recent years, much attention has been paid to the global consistency of normal orientations, such as Stochastic Poisson Surface Reconstruction (SPSR) [Sellán and Jacobson 2022], iterative Poisson Surface Reconstruction (iPSR) [Hou et al. 2022] and Parametric Gauss Reconstruction (PGR) [Lin et al. 2022]. For example, iPSR repeatedly refines the surface by feeding the normals computed in the preceding iteration into the Poisson surface reconstruction solver. PGR treats surface normals and surface element areas as unknown parameters, facilitating the Gauss formula to interpret the indicator as a member of some parametric function space. Global methods achieve better results than local methods. However, they still suffer from data sparsity coupled with nearby gaps, thin-walled structures or highly complex geometry/topology. For example, iPSR may disconnect thin structures while PGR may generate bulges for tubular shapes. Furthermore, PGR's application on large models is constrained by the super-linear growth of GPU memory.

Regression-based Approaches. Regression-based methods model normal estimation as a regression or classification task where the surface normals are directly regressed from the feature extracted from the local patches. Specifically, PCPNet [Guerrero et al. 2018] encodes the multiple-scale features of local patches in a structured manner, which enables one to estimate local shape properties such as normals and curvature. Nesti-Net [Ben-Shabat et al. 2019] estimates the multi-scale property of a point on a local coarse Gaussian grid, which defines a suitable representation for the CNN architecture and enables accurate normal estimation. Zhou et al. [2020]

proposed a multi-scale selection strategy to select the most suitable scale for each point through a joint analysis of multiscale features. Hashimoto and Saito [2019] used a point network and a voxel network to estimate normal vectors without sacrificing the inference speed. Although the regression-based methods typically outperform traditional data-independent methods, the regression-based methods rely on a large amount of training data for network training and are limited by the generalization capability because the brute-force training course may cause the network to overfit the normal vectors from the training data.

Surface fitting-based approaches. Different from those regressionbased methods, surface fitting-based approaches estimate a fitting surface by taking advantage of its neighboring points. In particular, Lenssen et al. [2020] presented a light-weight graph neural network that parameterizes a local quaternion transformer and a deep kernel function to iteratively re-weight graph edges in a large-scale point neighborhood graph. DeepFit [Ben-Shabat and Gould 2020] achieves scale-free normal estimation by per-point weight estimation for weighted least squares. Zhu et al. [2021] predicted an additional offset to improve the quality of normal estimation. Recently, the dipole propagation [Metzer et al. 2021] establishes a consistent normal orientation in a local phase and a global phase. However, tests show that dipole cannot deal with the point sparsity or tubular

Although deep learning approaches show great potential in normal estimation, it is still notoriously hard for both point-based regression approaches and surface fitting-based approaches to robustly deal with different noise levels, outliers, thin-plate structures, and varying levels of detail.

Voronoi-based Normal Orientation

Voronoi diagrams, as a powerful tool to encode spatial proximity, are extensively used to estimate normal vectors [Alliez et al. 2007; Amenta and Bern 1998; Boltcheva and Lévy 2017; Dey and Goswami 2004; Dey et al. 2005; Grimm and Smart 2011; Kolluri

et al. 2004; Mérigot et al. 2010; OuYang and Feng 2005; Wang et al. 2012]. Amenta and Bern [1998] proved that when the point density satisfies the standard of local feature size, one can roughly recover the real normals and even construct a discrete interpolation-type surface that is conformal to the base surface. The central idea is to identify inside poles and outside poles from the Voronoi diagram of the input point cloud, and use the poles to help orient the point cloud and assign their normals. Observing the Voronoi diagram can locally represent the most likely direction of the normal to the surface, Alliez et al. [Alliez et al. 2007] proposed to compute an implicit function by solving a generalized eigenvalue problem. It can be seen from the existing approaches that inside poles and outside poles are robust to noise, which helps find the dominant Delaunay balls in a noise-resistant manner [Dey and Goswami 2004]. Generally speaking, Voronoi diagrams can produce faithful results for dense point clouds but are weak in dealing with thin-plate structures or sharp features. In this paper, we thoroughly investigate the winding number by analyzing all the Voronoi vertices of the input point cloud. Our approach utilizes the winding-number requirements to ensure global normal consistency while relying on the Voronoi diagram to accurately predict the normals.

2.3 Winding Number

The winding number was first introduced by [Meister 1769]. For a smooth manifold surface, it can be computed using a contour integral in complex analysis. As a powerful tool for inside-outside tests, it has been widely used in many higher-level geometry processing operations including tetrahedral meshing [Hu et al. 2020], reconstruction [Barill et al. 2018; Wang et al. 2022b], normal orientation for point clouds [Metzer et al. 2021], shape analysis [Wang et al. 2022a], shape modeling [Sellán et al. 2021], animation [Nuvoli et al. 2022]. For example, Jacobson et al. [2013] introduced a winding-number-based function to guide an inside-outside segmentation of a polygonal surface.

Barill et al. [2018] derived a differential form of the winding number function and gave a tree-based fast algorithm to reduce the asymptotic complexity of generalized winding number computation, and also demonstrated a variety of new applications.

It's known that if the input point cloud is equipped with a meaningful normal setting, the winding number can robustly distinguish the inside from the outside in a global manner and is valued at 1 (inside) and 0 (outside). This observation motivates us to regularize the winding-number field by repeatedly tuning the normals so that they become consistent.

3 PRELIMINARIES

3.1 Generalized Winding Number

The theory of winding number can be generalized to polygonal meshes [Jacobson et al. 2013], triangle soup and point clouds [Barill et al. 2018]. Suppose $\{\mathbf{p}_i\}_{i=1}^N$ are samples from a continuous surface with normals $\{\mathbf{n}_i\}_{i=1}^N$. The generalized winding number w at the query point \mathbf{q} can be expressed as an area-weighted sum of the

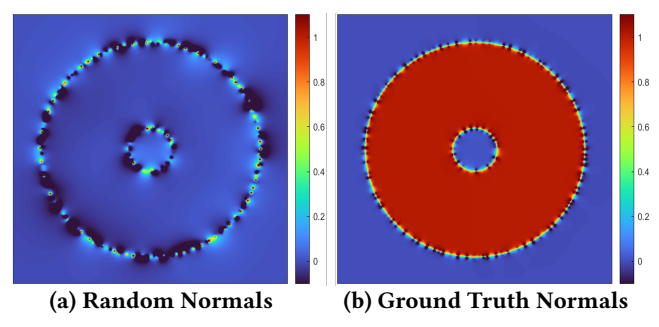
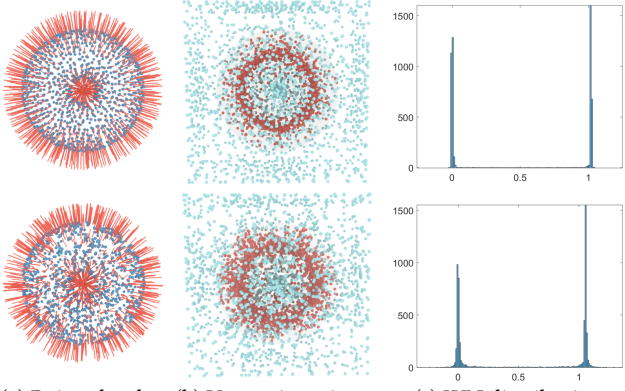


Fig. 4. (a) If the normals are random, the winding number tends to be 0 everywhere. (b) If the normals can encode a closed and orientable shape, the winding number is valued at 1 (interior) and 0 (exterior).



(a) Point cloud (b) Voronoi vertices (c) WN distribution
Fig. 5. Assuming the point cloud is equipped with a ground-truth normal

setting, we examine the winding number at the Voronoi vertices of the point cloud. Top row: For a noise-free point cloud, the winding number is close to either 0 or 1 for Voronoi vertices. Bottom row: When noises are added to point positions, the histogram of the winding number has a slight change, but still demonstrates two peaks close to 0 and 1. Note that the intersection points between the Voronoi edges and the 1.3x bounding box are also included for the winding number query.

overall contribution of the point set [Barill et al. 2018]:

$$w(\mathbf{q}) = \sum_{i=1}^{N} a_i \frac{(\mathbf{p}_i - \mathbf{q}) \cdot \mathbf{n}_i}{4\pi \left\| (\mathbf{p}_i - \mathbf{q}) \right\|^3},$$
 (1)

where a_i is the dominating area of the point \mathbf{p}_i . Obviously, the normals are central to the computation of winding numbers. When the normals are random, see Fig. 4 (a), the winding number tends to be 0 everywhere. If the normals can encode a closed and orientable shape, instead, see Fig. 4 (b), the winding number is about 1 for the interior points and 0 for the exterior points.

Remark: How to estimate a_i is a problem when the base surface is not available. A commonly used technique [Barill et al. 2018] is to project \mathbf{p}_i 's k-nearest neighbors onto the tangent plane of \mathbf{p}_i . Thus a_i is approximated by the area of the \mathbf{p}_i 's cell of the 2D Voronoi diagram. However, this strategy depends on the choice of k. Since the estimation of a_i is essential to the computation of the winding number, we adopt a parameter-free strategy in Sec. 4.4.

3.2 Voronoi Vertices for Examining Winding Number

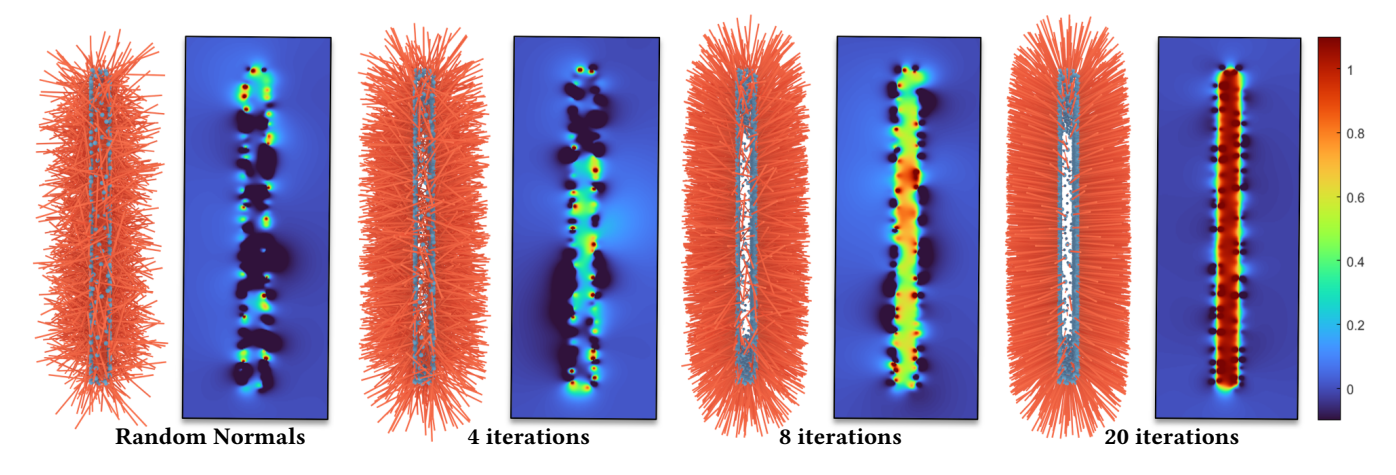
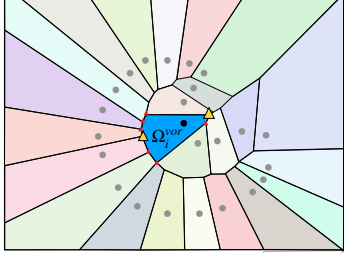


Fig. 6. The optimization progress using our method. The input model is a thin board with randomly initialized normals (in orange) of the point cloud. We cut the board in the middle with a plane to show the sectional view of the winding-number field (visualized in a color-coded style).

The Voronoi diagram (VD) of a set of points $\{p_i\}_{i=1}^N$ partitions the entire space into Ncells based on spatial proximity. In 3D, it includes Voronoi vertices, Voronoi edges, Voronoi faces, and Voronoi cells as the atomic elements. Let



 Ω_i^{vor} be the cell of \mathbf{p}_i ; See the 2D example in the inset figure. The two farthest vertices of Ω_i^{vor} , located on both sides of the surface, are defined as poles [Amenta et al. 2001], which are helpful for orienting normals. Note that the inside poles and the outside poles are hard to be distinguished before the normals are determined. Therefore, in this paper, we use all the Voronoi vertices, a superset of the Voronoi poles, for examining the winding number given by a point cloud.

As shown in the top row of Fig. 5(c), the winding number is close to either 0 or 1 at the Voronoi vertices for a noise-free point cloud. If we add noises to point positions at a level of 0.5%, the histogram just changes slightly (see the top row of Fig. 5(c)). Note that in Fig. 5 (b), the Voronoi vertices are colored in red (resp. cyan) if the winding number is close to 1 (resp. 0). Besides, we use a 1.3x bounding box to enclose the point cloud and add the intersection points between the Voronoi edges and the box as examination points. One may consider a different strategy for generating the examination points, e.g., adding Gaussian noise to the input point cloud. Based on our tests, most of the Voronoi vertices are remote from the surface and noise-insensitive, which accounts for why we take the Voronoi vertices as examination points. We conduct the ablation study in Supplementary Material.

METHOD

The winding number, in its nature, can reflect global inside-outside information, which motivates us to compute the normals by regularizing the winding-number field. In the implementation, we examine the winding number at the Voronoi vertices of the point cloud. We

hope that the computed normals can not only lead to a reasonable winding-number field but also accurately align with Voronoi poles. The requirements can be summarized into the following three aspects.

 $w(\mathbf{q})$ is valued at 0 or 1. Although one can construct a surface such that the winding number is valued at any integer, we only consider the common case where the winding number is either 0 or 1. We shall include a term $f_{01}(\mathbf{n})$ to characterize the basic requirement of a valid winding-number field.

The winding-number values are balanced for \mathbf{p}_i 's Voronoi vertices. Sample \mathbf{p}_i dominates a cell in the Voronoi diagram. In general cases, it is unlikely that all the Voronoi vertices of p_i 's cell are located inside or outside. Therefore, we hope the number of 1's and the number of 0's are balanced when we consider the winding number of \mathbf{p}_i 's Voronoi vertices. This observation leads to a balance term $f_B(\mathbf{n})$.

Normals align with Voronoi poles. Like the power crust techniques [Amenta et al. 2001], Voronoi poles are very helpful in predicting the normals. Let \mathbf{q}_k^i be the k-th Voronoi vertex of \mathbf{p}_i 's Voronoi cell. We hope the vector $\mathbf{q}_k^i - \mathbf{p}_i$ has similar orientation with \mathbf{n}_i if $w(\mathbf{q}_{k}^{i}) \approx 0$ but reverse orientation with \mathbf{n}_{i} if $w(\mathbf{q}_{k}^{i}) \approx 1$. The alignment requirement leads to a term $f_A(\mathbf{n})$.

By summarizing them together, we get a functional w.r.t. the normals,

$$f(\mathbf{n}) = \frac{f_{01}(\mathbf{n}) + \lambda_B f_B(\mathbf{n}) + \lambda_A f_A(\mathbf{n})}{N},$$
 (2) where λ_B and λ_A are two parameters to tune the influence of f_B and

 f_A , respectively. We establish the details of the separate terms in the following subsections, while delaying the ablation study of λ_B and λ_A in supplementary material. Fig. 6 gives an example of how the normals change with the decreasing of the value of f.

4.1 The 0-1 Term f_{01}

Double well function. In the continuous setting, the winding number is valued at 0 or 1 if the input surface is closed and topologically equivalent to a single-layer orientable surface. Therefore, we need to

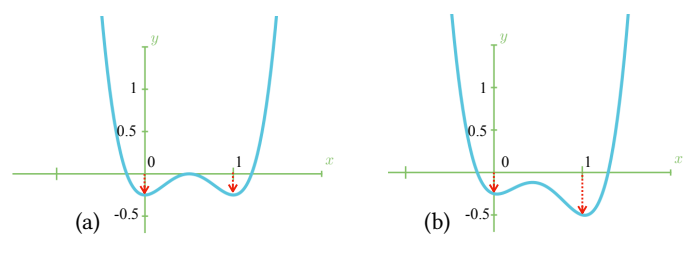


Fig. 7. (a) A standard double well function. (b) A new version with a shear correction for suppressing the randomness of normals.

define an energy function to pull the winding number to the binary states as far as possible. For this purpose, we introduce the double well function inspired by one of the most important functions in the field of quantum mechanics [Jelic and Marsiglio 2012]. A simple form of the double well function can be written as:

$$f_{DW}(x) = 4(x - 0.5)^4 - 2(x - 0.5)^2,$$
 (3)

with two valleys at x = 0 and x = 1, respectively, as Fig. 7(a) shows.

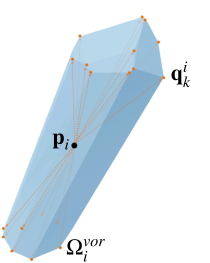
A new double well function with a shear correction. If we equip a point cloud with a set of random normals, the resulting winding number tends to be 0 for an arbitrary query point; See Fig. 4(a). In order to encourage the occurrence of 1's for the winding number of examination points, we need to tune the double well function with a shear correction, as Fig. 7(b) shows. In this way, the 0-1 term f_{01} can be defined by the overall contribution of the winding number $w_i = w_i(\mathbf{n})$ at \mathbf{q}_i , $i = 1, 2, \dots, M$.

$$f_{01}(\mathbf{n}) = \sum_{j}^{M} \left(f_{DW}(w_j) - \frac{w_j}{D} \right), \tag{4}$$

where the parameter D is used to tune the degree of shear correction. We make the ablation study about D in the supplementary material and empirically set D=4 for all the experiments.

4.2 The Balance Term f_B

Let Ω_i^{vor} be the Voronoi cell dominated by the point \mathbf{p}_i of the point cloud. If the point density meets the local feature size standard [Amenta and Bern 1998], one half of Ω_i^{vor} is located inside the surface, and the other half is located outside. Therefore, it is reasonable to suppress the occurrence of the situation that all vertices of Ω_i^{vor} are inside the shape or outside the shape. In other words, the winding-



number scores at the vertices of Ω_i^{vor} should be balanced, which can be achieved by maximizing the variance of the winding-number scores. Let \overline{w}^i be the average score for Ω_i^{vor} . The variance can be measured by $\sum_k^{M_i} (w_k^i - \overline{w}^i)^2$, where M_i is the total number of vertices of Ω_i^{vor} , and $w_k^i = w(\mathbf{q}_k^i)$ is the winding-number score for the k-th vertex \mathbf{q}_k^i . The balance term can be defined by the overall winding-number variance.

$$f_B(\mathbf{n}) = -\sum_{i}^{N} \left(\frac{1}{M_i} \sum_{k}^{M_i} (w_k^i - \overline{w}^i)^2 \right).$$
 (5)

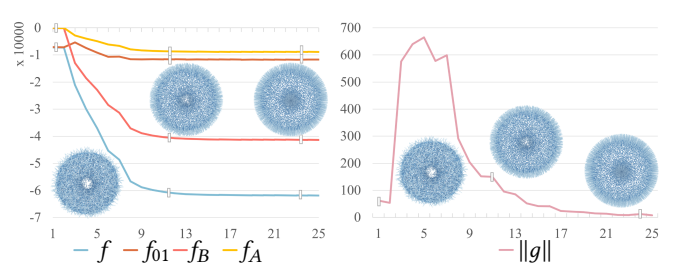


Fig. 8. Plot on the decreasing of the functional value and the gradient norm. The experiment is made on the torus model with 4K points.

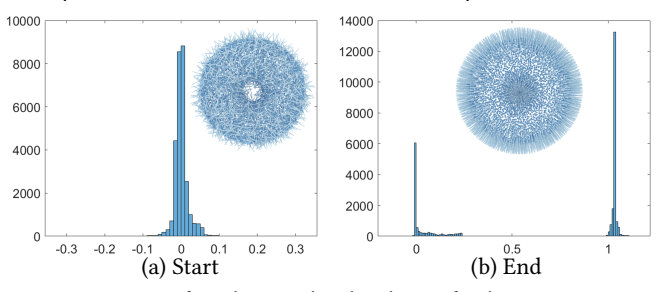


Fig. 9. Histograms of winding number distribution for the Voronoi vertices of the torus point clouds, before and after optimization. It can be seen that the distribution of the winding number is regularized by optimization.

4.3 The Alignment Term f_A

As pointed out in [Amenta and Bern 1998], Voronoi poles are useful for orienting the normals. Let \mathbf{p}_i be a point in the given point cloud, \mathbf{p}_i 's Voronoi cell Ω_i^{vor} has M_i vertices, i.e., \mathbf{q}_k^i , $k=1,2,\cdots,M_i$. If \mathbf{q}_k^i is the inside (resp. outside) pole of \mathbf{p}_i , $\mathbf{p}_i-\mathbf{q}_k^i$ (resp. $\mathbf{q}_k^i-\mathbf{p}_i$) approximately aligns with the normal vector of \mathbf{n}_i . In this paper, we turn the observation into an alignment requirement by enforcing the two sequences

$$\mathbf{n}_i \cdot (\mathbf{q}_k^i - \mathbf{p}_i), \quad k = 1, 2, \cdots, M_i$$

and

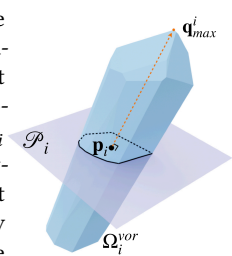
$$w_k^i$$
, $k = 1, 2, \cdots, M_i$

to have exactly the reverse ordering. According to the rearrangement inequality [Hardy et al. 1952], we hope $\sum_k^{M_i} w_k^i \mathbf{n}_i \cdot (\mathbf{q}_k^i - \mathbf{p}_i)$ to get minimized. Therefore, we can define the alignment term as follows.

$$f_A(\mathbf{n}) = \sum_{i}^{N} \left(\frac{1}{M_i} \sum_{k}^{M_i} w_k^i \mathbf{n}_i \cdot (\mathbf{q}_k^i - \mathbf{p}_i) \right). \tag{6}$$

4.4 Implementation Details

Area weight of \mathbf{p}_i . Let \mathbf{p}_i be a point in the given point cloud. The estimation of the winding number at an arbitrary point has to input the weighting area of \mathbf{p}_i ; See Eq. (1). A typical way for defining the weighting area a_i is based on KNN [Barill et al. 2018]. However, it has to include a parameter k to resist the irregular distribution of points (typically k=20). In this paper, we use a parameter-free



strategy for estimating a_i . As the inset figure shows, $\mathbf{q}_{max}^i \in \Omega_i^{vor}$

Sampling White Noise Sampling without noise White Noise Sampling With 0.25% noise White Noise Sampling With 0.5% noise Models PGR PCPNet Dipole PCPNet Dipole PGR Hoppe König PCPNet Dipole iPSR Ours Hoppe König PGR iPSR Ours Hoppe König iPSR Ours 82-block 99,730 99,980 89 300 97.080 99 275 99,175 99,980 84.980 99,900 89.750 98.030 98,800 98.150 99,930 98,950 99,730 89.030 98.230 97.350 98,000 99.880 94.350 99.580 bunny chair 69.580 86.730 86.030 80.580 100.000 99.975 100.000 88.030 85.880 86.480 73.550 99.975 100.000 100.000 72.830 65.05 86.430 77.450 99.275 99.400 99.400 cup-22 68,450 55.980 68,350 56.230 99.925 99 950 55.930 67.700 99.350 98.725 99.850 61.180 60.780 93,400 59 380 60.100 cup-35 99.800 59.880 83.400 54.400 100.000 100.000 100.000 99.530 60.780 83.00 52.430 99.900 99.950 100.000 99.000 60.830 82.100 53.030 98.725 99.950 100.000 fandisk 98.880 99.850 96.880 86,750 99,725 100.000 99,480 99,900 96,800 86.700 99,650 99.050 99.950 97.530 99,580 96,850 95,800 98.850 97.325 99.750 holes 100.000 100.000 100.000 94.600 100.000 91.000 100.000 94.830 100.000 100.000 100.000 100.000 100.000 95,930 90.780 99,425 99,500 99.800 92,680 90,700 95,550 93.080 99,250 99.325 99,750 93,630 89.880 95,530 89,630 96.850 98.425 97,500 95.700 94.100 98.230 99.750 100.000 100.000 99.980 69.980 93.730 99,980 99.850 99.980 80.780 56.230 99.925 100.000 99.980 81.380 98.725 100.000 100.000 99.780 80.600 70.530 95.300 100.000 89,980 97,750 94.580 94.880 93.400 93.500 88.450 88.880 94.830 mobius 100.000 55.150 89.800 53.950 100.000 87.250 100.000 68.600 55.130 86.980 54.200 99.175 80.525 99.380 55.980 55.130 82.030 53.650 94.900 68.225 85.780 66 980 77 350 68 250 99 925 99 875 100 000 98 480 67 480 77 330 67 000 99 925 99 900 100 000 68 230 68 000 76 930 66 150 99.050 99 700 100 000 mug octa-flower 98 450 50.900 88.030 95.300 98.600 95.350 99.330 53.800 95.180 97.725 95.525 98.800 89.330 86.930 98.200 95.500 96.225 93.775 98.550 58.180 99.000 99.280 sheet 51.200 51.130 83,980 52,450 100.000 99.075 100.000 99,480 51.300 83,400 52,700 99,950 98.950 100.000 51.100 51.050 81.130 59.550 99.875 97.225 99,980 torus trimstar 100.000 91.050 96.700 99.650 100.000 100.000 90.930 94.350 98.150 98.880 100.000 91.080 94.830 98.500 75.980 99.100 99.825 100.000 83.130 82.480 99.000 99.475 99.650

Table 1. Statistics on the truth percentages under different sampling conditions and noise levels.

is the farthest Voronoi vertex to p_i . We build a plane orthogonal to $\mathbf{q}_{max}^i - \mathbf{p}_i$ and use it to cut Ω_i^{vor} into two halves, resulting in a convex cut polygon. We use the area of the cut polygon to define a_i .

Optimization details. The overall objective function takes the normals \mathbf{n}_i , $i = 1, 2, \dots, N$, as variables. As \mathbf{n}_i is required to be a unit vector, we parameterize a normal vector as

$$\mathbf{n}_i = (\sin(u_i)\cos(v_i), \sin(u_i)\sin(v_i), \cos(u_i)). \tag{7}$$

In this way, we turn the problem of minimizing $f(\mathbf{n})$ into an unconstrained optimization problem.

The function $f = f(\mathbf{n})$ can be viewed as a composite function of

$$f = f(w_1, w_2, \cdots, w_M)$$

and

$$w_i = w_i(\mathbf{n}_1, \mathbf{n}_2, \cdots, \mathbf{n}_N).$$

At the same time, \mathbf{n}_i is a composite function of u_i and v_i . Therefore, the gradients of the overall function can be quickly computed by the chain rule. We omit the form of the detailed gradients for brevity. Fig. 8 plots how the objective function and the gradient norm are decreased during the optimization. It can be seen from Fig. 9 that the normals become globally consistent upon the regularization of the winding number.

Remark. In order to show that the minimization of f can arrive at the termination, we need to prove the fact that the objective function has a lower bound. Observing that f_{01} is quartic about w_i (with a positive leading coefficient) but the other two terms have a lower degree, it is easy to know that f approaches $+\infty$ if one of the winding numbers is sufficiently large, which naturally constrains every w_i in a limited range, e.g., $[W_1, W_2]$. Therefore, the boundedness of f follows immediately from the boundedness of w_i . See more rigorous proof in the supplemental material.

EXPERIMENTAL RESULTS 5

Experimental Setting

Platform. Our experiments are conducted on a computer with an AMD Ryzen 9 5950X CPU and 32 GB memory. We run the GPUbased approaches [Guerrero et al. 2018; Li et al. 2022; Lin et al. 2022; Metzer et al. 2021; Zhu et al. 2021] on an NVIDIA GeForce RTX 3090 card.

Point clouds and Normalization. We make the tests on a total of 18 models of various shapes (see Table 1). All the point clouds are normalized to a range of $[-0.5, 0.5]^3$. We use two types of sampling strategies, i.e., white noise sampling and blue noise sampling [Jacobson et al. 2021]. Besides the noise-free point clouds, We scale all models to $[-0.5, 0.5]^3$ so that the longest edge of the bounding box is always 1.0. For noise generation, we use the standard Gaussian distribution with $\mu = 0.0$ and $\sigma^2 = 1.0$ to produce noise displacement. Each point is given a random displacement that is added to the original position. The noise level is controlled by a scale factor of 0.25% and 0.5%, respectively.

Parameters. In all the experiments, we adopt the same parameter setting: $\lambda_A = 10.0$, $\lambda_B = 50.0$, and D = 4.0. We use the L-BFGS algorithm implemented in C++ for solving the optimization. The termination condition is set by requiring the difference between the objective function values at two consecutive steps not to exceed a threshold of 1.0.

Approaches. We include five state-of-the-art (SOTA) methods [Guerrero et al. 2018; Hoppe et al. 1992; König and Gumhold 2009; Lin et al. 2022; Metzer et al. 2021] for comparison. PGR [Lin et al. 2022] receives an un-oriented point cloud as the input and outputs a polygonal surface, but we focus more on the quality of its computed normals. Note that [Hoppe et al. 1992] and [König and Gumhold 2009] need to pre-compute a Riemannian graph to encode the proximity between points. In our experiments, we take two closely spaced points as neighbors if the distance between them is less than 0.05. Besides, PCPNet [Guerrero et al. 2018] has multiple pre-trained models, we use multi_scale_oriented_normal in all experiments. For PGR [Lin et al. 2022] and Dipole [Metzer et al. 2021], we follow the default setting.

5.2 Comparisons

Indicators. We evaluate the performance from two aspects. On the one hand, we keep track of the percentage of correctly oriented normals. For an input point p_i , the predicted orientation is true if the angle between the computed normal and the ground-truth normal is less than 90 degrees. On the other hand, we make statistics about the reconstruction quality by feeding the point clouds and the normals together into the SPR solver [Kazhdan et al. 2006]. Specially,

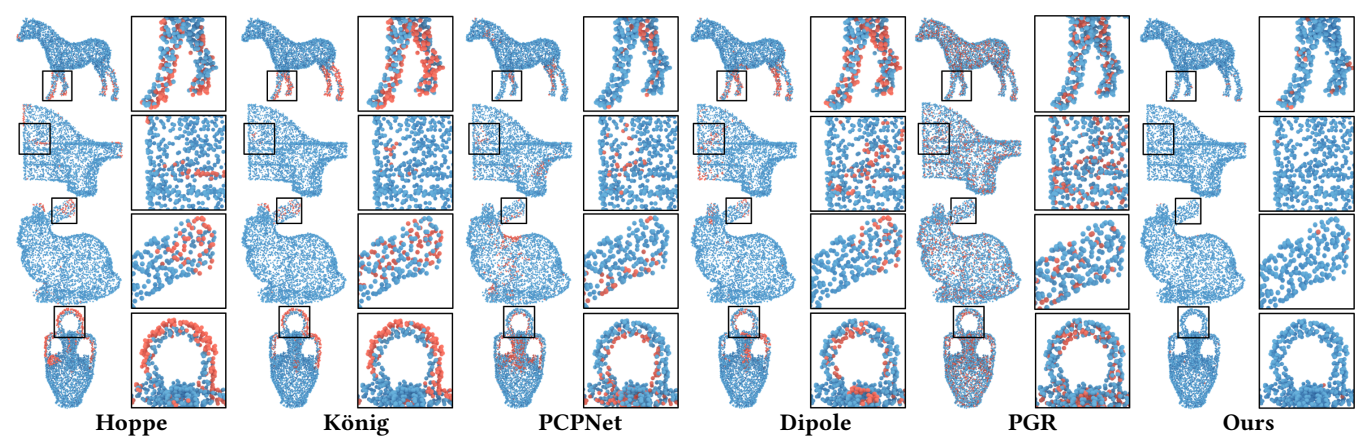


Fig. 10. Comparison on the ratio of true normals between our approach and the existing five methods: Hoppe [Hoppe et al. 1992], König [König and Gumhold 2009], PCPNet [Guerrero et al. 2018], Dipole [Metzer et al. 2021] and PGR [Lin et al. 2022]. The true predictions and false predictions are colored in blue and red, respectively. Note that the level of Gaussian noise is 0.5%.

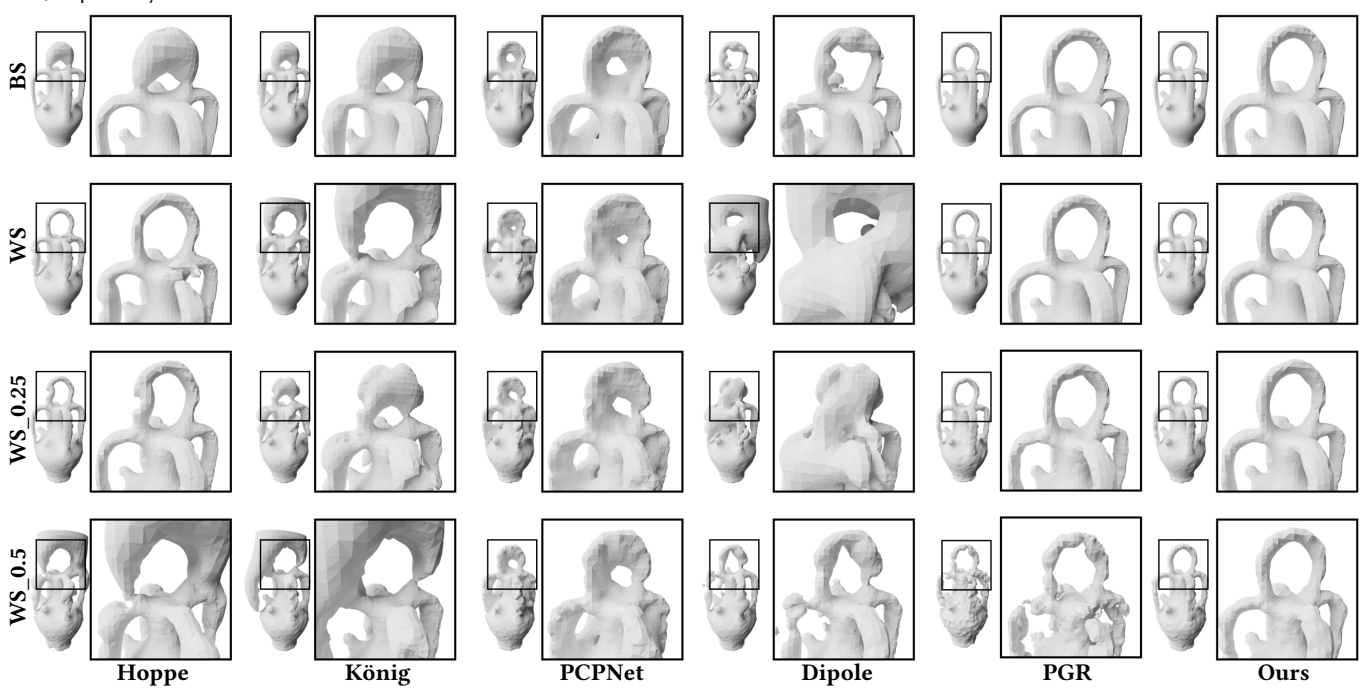


Fig. 11. Visual comparison of the reconstructed surfaces at different sampling conditions and different levels of noise. We show results of four different sampling conditions: BS (blue noise sampling), WS (white noise sampling), WS_0.25 (white noise sampling with 0.25% noise) and WS_0.5 (white noise sampling with 0.5% noise).

we use the *Chamfer Distance* (CD) to measure the error between the ground-truth surface and the reconstructed surface (with the support of predicted normals).

Quality of predicted normals. In Table 1, we show the statistics of the truth percentages of normals over the 18 models, under different sampling conditions and noise levels. The statistics show that our approach has a higher truth percentage than the SOTA methods. For example, for the blue noise sampling point clouds, our approach can achieve a percentage of 100% for 88.9% of the tested models, much higher than the SOTA methods. Furthermore, we give a visual

comparison in Fig. 10 where the points are colored differently depending on whether the normal orientation is correctly predicted. It can be clearly seen that our approach has an advantage in predicting the normals for points in the tubular regions and thin regions with sharp features and corners; See the highlighted regions.

Besides, we also make statistics about the Root Mean Square Error (RMSE) of angles between the estimated normal and the ground-truth normal, which also shows that our algorithm has advantage in prediction accuracy. The detailed statistics are included in the supplementary material.

Table 2. Reconstruction quality comparison using Poisson surface reconstruction solver [Kazhdan et al. 2006] with predicted normals. The Chamfer Distance between the reconstructed surface and the ground-truth surface is presented scaled by a factor of 100 for a better presentation.

Sampling	White Noise Sampling without noise					White Noise Sampling With 0.25% noise						White Noise Sampling With 0.5% noise									
Models	Hoppe	König	PCPNet	Dipole	PGR	iPSR	Ours	Hoppe	König	PCPNet	Dipole	PGR	iPSR	Ours	Hoppe	König	PCPNet	Dipole	PGR	iPSR	Ours
82-block	0.149	0.149	0.489	0.195	0.158	0.165	0.130	0.593	0.155	0.521	0.184	0.202	0.195	0.134	0.175	0.172	0.578	0.203	0.462	0.244	0.184
bunny	0.143	0.230	0.326	0.358	0.092	0.103	0.112	0.130	0.285	0.355	0.354	0.173	0.156	0.126	0.198	0.285	0.379	0.280	0.322	0.203	0.157
chair	1.758	0.739	0.425	0.583	0.118	0.074	0.076	0.599	0.761	0.461	0.912	0.166	0.116	0.080	1.545	2.311	0.516	0.795	0.397	0.165	0.172
cup-22	1.673	1.631	1.523	1.787	0.121	0.131	0.112	0.338	1.680	1.539	1.778	0.203	0.191	0.139	1.898	1.715	1.568	1.764	0.347	0.267	0.193
cup-35	0.133	1.221	0.903	1.613	0.095	0.115	0.098	0.119	1.215	0.884	1.771	0.171	0.170	0.094	0.147	1.278	0.979	1.721	0.297	0.214	0.134
fandisk	0.128	0.123	0.195	0.637	0.081	0.090	0.073	0.127	0.126	0.211	0.643	0.149	0.120	0.103	0.191	0.171	0.254	0.219	0.307	0.181	0.169
holes	0.036	0.036	0.252	0.286	0.072	0.075	0.073	0.039	0.039	0.267	0.200	0.191	0.144	0.070	0.051	0.051	0.328	0.254	0.576	0.193	0.149
horse	0.291	0.482	0.165	0.307	0.085	0.082	0.075	0.281	0.465	0.192	0.224	0.167	0.088	0.090	0.305	0.522	0.238	0.358	0.454	0.244	0.178
kitten	0.064	0.061	0.268	0.076	0.061	0.099	0.088	0.066	0.065	0.265	0.079	0.177	0.109	0.084	0.073	0.072	0.299	0.092	0.319	0.161	0.144
knot	0.040	0.040	0.817	1.634	0.166	0.105	0.064	0.045	0.046	0.822	0.998	0.338	0.140	0.068	0.063	0.311	0.875	0.931	0.652	0.191	0.123
lion	0.229	0.351	0.211	0.397	0.112	0.117	0.087	0.268	0.349	0.224	0.248	0.268	0.198	0.112	0.388	0.383	0.274	0.365	0.619	0.251	0.228
mobius	0.117	1.551	0.563	1.507	0.126	0.156	0.237	2.161	1.549	0.649	1.529	0.238	0.287	0.417	2.819	1.743	0.755	1.607	0.410	0.435	0.634
mug	0.135	1.228	1.208	1.506	0.135	0.906	0.125	0.146	1.238	1.214	1.514	0.214	0.929	0.118	1.276	1.244	1.253	1.624	0.322	1.240	0.146
octa-flower	2.424	0.601	0.130	0.245	0.093	0.139	0.164	2.445	1.505	0.146	0.232	0.193	0.165	0.177	0.521	0.703	0.181	0.238	0.372	0.293	0.247
sheet	1.607	1.613	3.327	1.563	0.098	0.650	0.091	0.123	1.607	2.909	1.511	0.167	0.717	0.116	1.630	1.635	3.046	1.545	0.380	0.881	0.219
torus	0.019	0.019	0.215	0.019	0.054	0.163	0.043	0.026	0.026	0.232	0.021	0.135	0.190	0.064	0.044	0.044	0.250	0.033	0.264	0.240	0.125
trimstar	0.214	0.137	0.417	0.175	0.158	0.147	0.112	0.154	0.142	0.422	0.208	0.340	0.153	0.110	0.158	0.153	0.454	0.238	0.670	0.225	0.170
vase	0.217	0.440	0.613	0.950	0.094	0.119	0.092	0.243	0.446	0.654	0.611	0.198	0.149	0.107	0.588	0.581	0.727	0.326	0.503	0.194	0.189

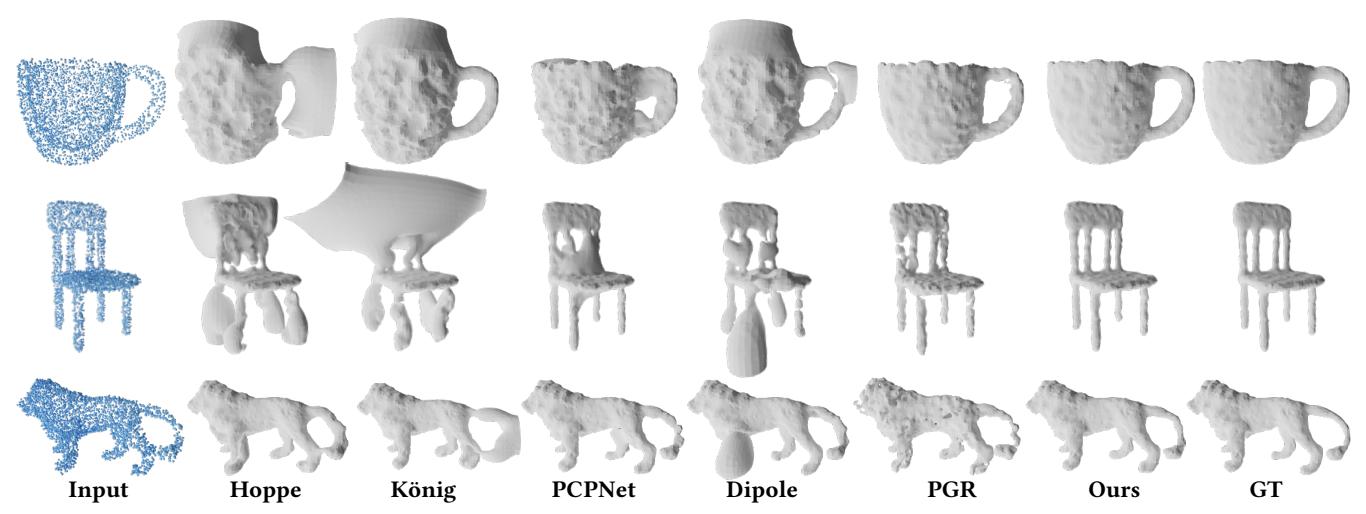


Fig. 12. Comparing the reconstruction quality on point clouds with 0.5% Gaussian noise.

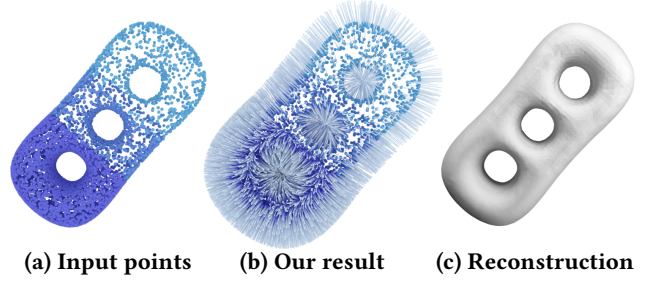


Fig. 13. We construct a point cloud of the genus-3 torus with varying point densities (colored in varying darkness). Both the predicted normals and the reconstructed surface show that our approach is robust to the point density.

Quality of reconstructed surfaces . We further take the SPR solver as a blackbox to observe the reconstruction quality. For a fair comparison, we capture the normals of PGR [Lin et al. 2022] and feed the oriented point set into the SPR solver. In fact, the original reconstruction strategy of PGR uses iso-surfacing to extract reconstructed surfaces and tends to produce over-smooth results. By comparison,

SPR is better than iso-surfacing in preserving geometric details for normals of the same quality. A basic fact is that better normals lead to better-reconstructed surfaces. We record the statistics about the reconstruction quality in Table 2. Note that the Chamfer Distance between the reconstructed surface and the ground-truth surface is scaled by 100 times for a better presentation. The statistics show that for most of the 18 models, our predicted normals produce the best reconstruction quality. For example, when the point sets are added by 0.5% Gaussian noise, our method has the best scores on 55% of the models. Based on the scores, the three top-ranked approaches are ours, König [König and Gumhold 2009] and Hoppe [Hoppe et al. 1992], respectively.

Furthermore, we use Fig. 11 to visually compare reconstruction results on the Vase model at various sampling conditions and noise levels. It can be seen that from the reconstructed surfaces our approach can infer the normals, with the highest fidelity. Especially, even if the noise level amounts to 0.5%, our method can still produce a faithful result; See the handles of the Vase model.

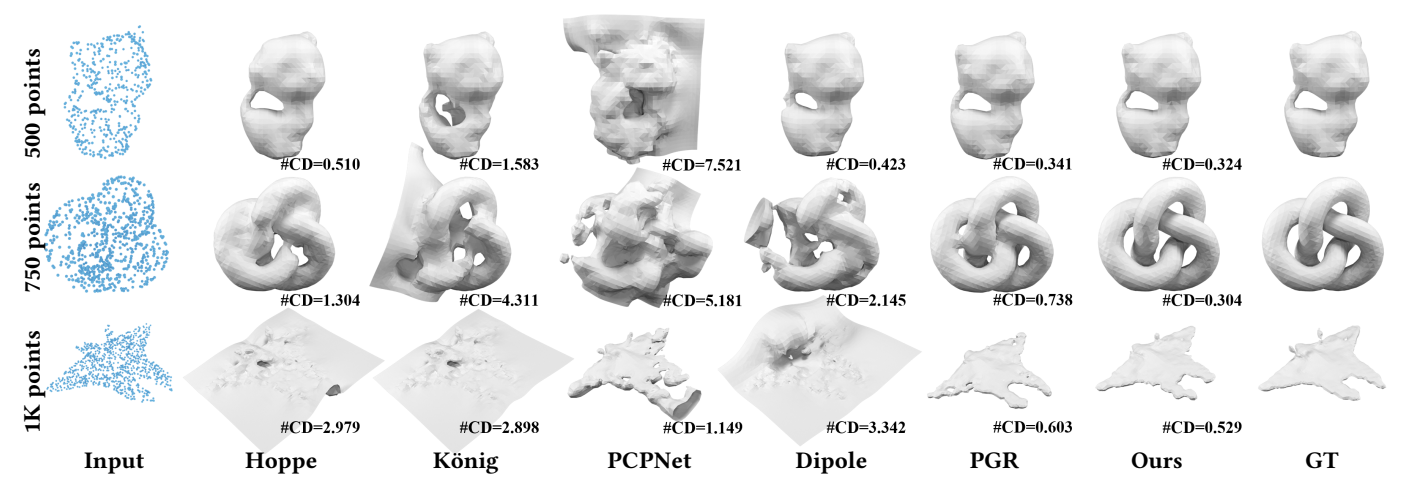


Fig. 14. Tests are made on sparse point clouds: 500 points, 750 points and 1K points. Our results are close to the ground truth for each of the three inputs. The comparison shows that our algorithm has a big advantage on sparse raw data. We also mark clearly the Chamfer Distance (CD) scores between the reconstructed surface and the ground-truth surface for a quantitative comparison. Note each CD score is scaled by a factor of 100.

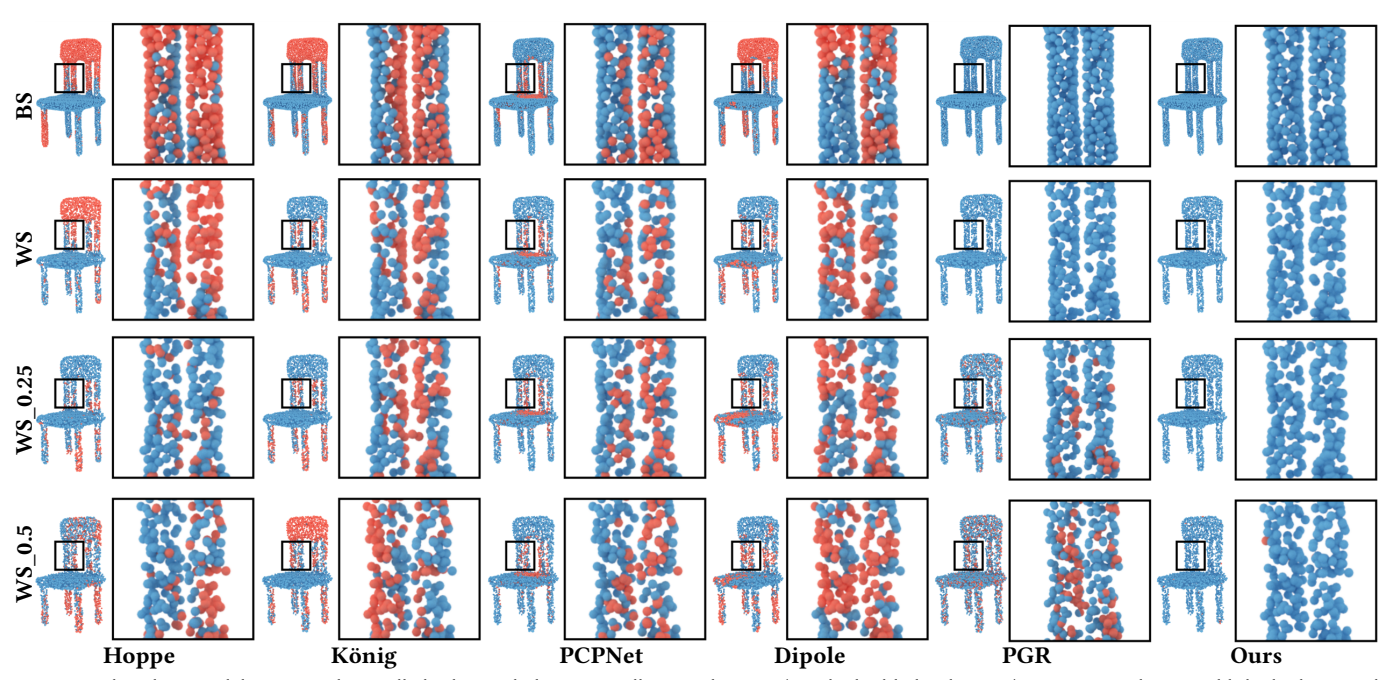


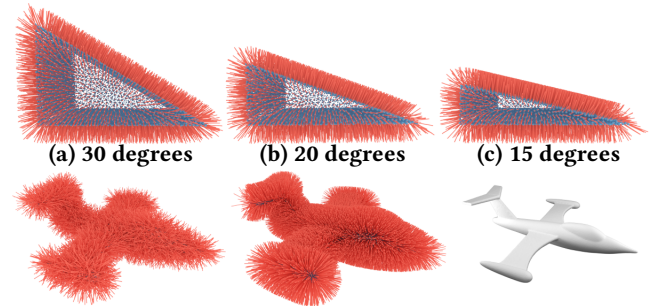
Fig. 15. The Chair model contains thin-walled tubes and plates, as well as nearby gaps (see the highlighted region). Our approach can yield the highest truth percentage among the five approaches. Note that the false predictions are colored in red.

5.3 Noise, Varying Point Density and Data Sparsity

Noise. In Fig. 12, we add 0.5% Gaussian noise to the point clouds of the Cup model, the Chair model, and the Lion model, to test the noise-resistant ability. It can be clearly seen from the visual comparison that our algorithm has a better noise-resistant ability. Specially, our algorithm can provide faithful normals on the back and the legs of the Chair model, even in presence of serious noise. Two reasons account for the noise-resistant property. First, we examine the winding number at the Voronoi vertices whose positions are robust to small variations of the original point cloud, especially

for those Voronoi vertices distant to the surface. Second, the whole optimization framework is built on the regularization of the winding number, and thus can capture the normal consistency from a global perspective.

Varying point density. In Fig. 13, we construct a point cloud with varying point density (colored in varying darkness). We intend to use this example to test if our algorithm can deal with irregular point distributions. Recall that Eq. (1) includes an area weight a_i , which has a serious influence on the estimation accuracy of the winding number. We give an intuitive technique for estimating a_i based on



(d) Random normals (e) Our result (f) Reconstruction

Fig. 16. (a-c) Our approach can estimate normals accurately even if the angles are as small as 15 degrees. (d-f) For the Airplane model with sharp angles, we show the initial normals, the optimized normals, and the faithfully reconstructed result.

the Voronoi diagram; See Section 4.4. The technique is parameterfree and computationally efficient. It can be seen from Fig. 13 that both the predicted normals and the reconstructed surface have a high quality, which shows that the estimation of a_i is independent of the point density.

Data sparsity. In Fig. 14, we have three sparse point clouds, and the numbers of points are respectively 500, 750, and 1K. We intend to use this example to test the performance on sparse inputs, since when there are nearby gaps and thin-walled tubes/plates, data sparsity will inevitably double the difficulty of predicting normals. It can be clearly seen from the visual comparison that our results are close to the ground-truth for each of the three inputs.

5.4 Nearby Gaps, Thin Plates/Tubes, and Sharp Angles

Nearby gaps and thin plates/tubes. For our approach, the strength in dealing with thin tubes has been validated on the Vase model shown in Fig. 11. In Fig. 15, we give four versions of the Chair point cloud to evaluate how well it handles nearby gaps and thin plates/tubes. As can be observed, our approach noticeably outperforms the SOTA methods in addressing these flaws (see the highlighted region), which is due to the global property inherited from the winding number.

Sharp angles. The existence of sharp angles is one of the challenges for orienting a raw point cloud. In the top row of Fig. 16, we show three toy models with different dihedral angles. It can be seen that our approach can estimate normals accurately even if the angles are as small as 15 degrees. We also use the Airplane model to test the ability to deal with sharp angles. Both the optimized normals and the faithfully reconstructed result show that our algorithm can produce a desirable result for point clouds with sharp angles. The contrast in the bottom row of Fig. 14 also validates the effectiveness of our approach in coping with sharp angles. It's worth pointing out that the propagation-based methods [Metzer et al. 2021] rely on the assumption of spatial coherence, which does not hold when sharp angles exist, and thus fail to fully capture the global context of the shape in presence of sharp angles.

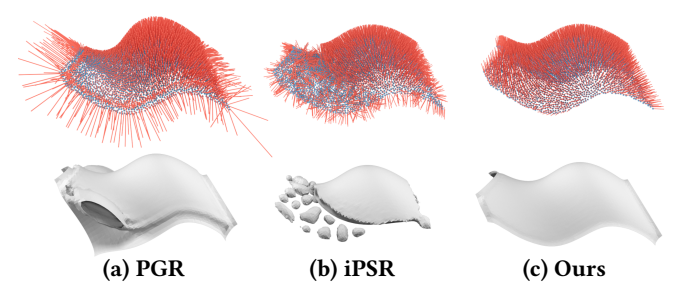


Fig. 17. Comparing PGR, iPSR, and ours on estimating normals for an opensurface point cloud. iPSR does not support open surfaces. PGR fails to report reliable normals for the boundary points. However, our estimated normals comply with the real shape at both the interior points and the boundary points.

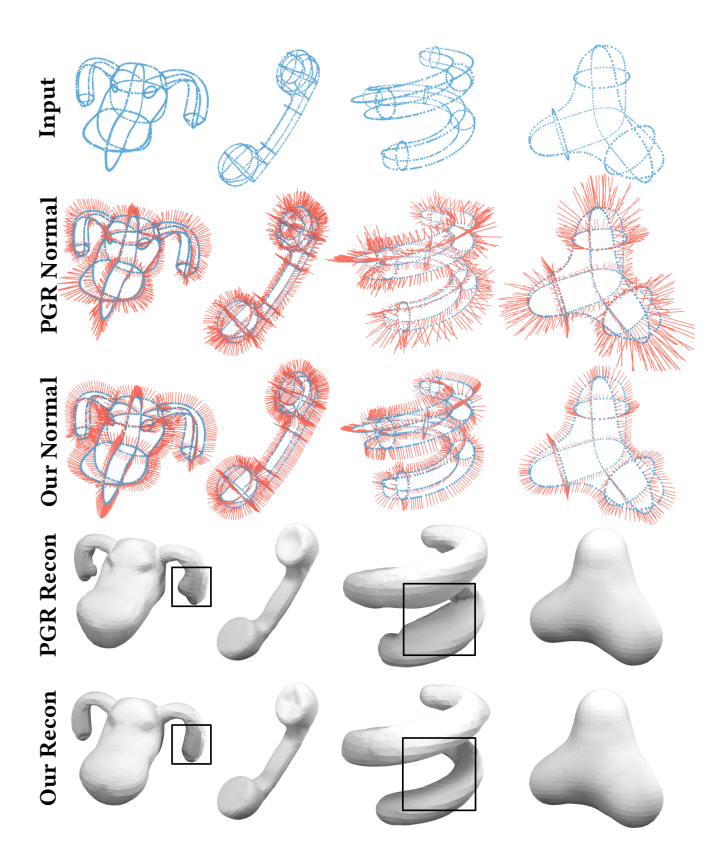


Fig. 18. Normal estimation for wireframe-type point clouds. All the models are from VIPSS [Huang et al. 2019]. PGR may produce bulges around thin tubular structures.

Open Surfaces, Wireframes, Complex Topology and Real Scans

Open-surface Point Cloud. In Fig. 17, we sample a point set from an open surface. We compare PGR, iPSR, and ours on estimating normals on the open-surface point cloud. iPSR does not support open surfaces. PGR fails to report reliable normals for the boundary points since it assumes the closed surface. In contrast, our estimated

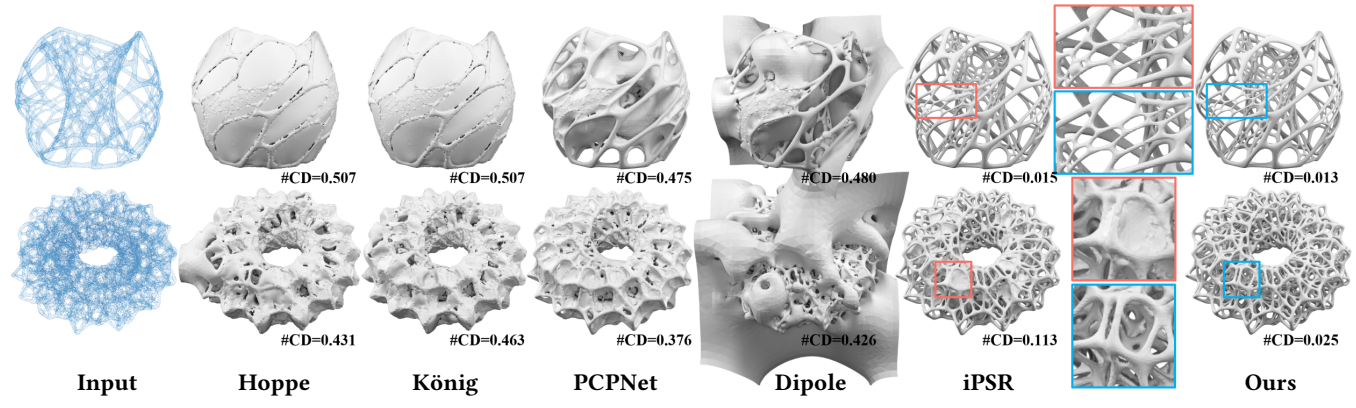


Fig. 19. Tests on point clouds with highly complex topology/geometry. The model in the top row has 80K points while the model in the bottom row has 100K points. Note that PGR runs out of GPU memory on an NVIDIA GeForce RTX 3090 graphics card. Chamfer Distance (CD) between the reconstructed surface and the ground-truth surface is marked for a quantitative comparison. Note each CD value is scaled by a factor of 100.

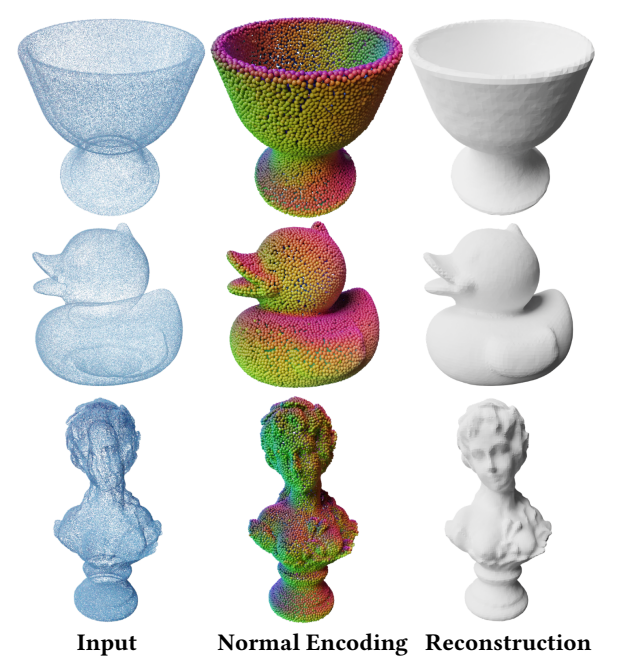


Fig. 20. The three raw point clouds are real scans downloaded from [Huang et al. 2022] dataset. Each of them is downsampled to 10K points. From the color-coded visualization of normals, as well as the reconstructed surfaces, we can see that our method can deal with real scans.

normals comply with the real shape at both the interior points and the boundary points.

On one hand, the winding number is still indicative for open surfaces [Chi and Song 2021; Jacobson et al. 2013]. On the other hand, the three terms in our objective function do not assume the closedness of the surface. Recall that we include the intersections between the 1.3x bounding box and the Voronoi diagram as examination points. If the input point set encodes a closed surface, it is proper to deem the intersections as outside points and enforce the winding number at the intersections to be 0. But for open surfaces,

the constraint cannot be specified. Therefore, in our implementation, we do not specify the requirements in all our experiments.

Wireframes. Wireframes serve as a kind of compact skeletal representation of a real-world object. Due to the extreme data sparsity, the SOTA methods fail to correctly predict the normals. Unlike patch-based normal fitting [Metzer et al. 2021], our approach aims at evaluating the global normal consistency by computing the overall contribution of each point. The experimental results in Fig. 18 show that both our method and PGR are capable of handling the wireframe-type inputs, but PGR may produce bulges around thin tubular structures (see the highlighted window).

Highly complex structures. Fig. 19 shows two nest-like models with complex topology/geometry. The point cloud in the top row has 80K points while the point cloud in the bottom row has 100K points. It can be seen that all five SOTA methods fail on the two highly complex models. iPSR [Hou et al. 2022] depends on the initialization of normals. For a shape with complicated topology/geometry, iPSR cannot reverse the false normals to the correct configuration, and thus easily cause disconnection or adhesion, especially around thin structures. PGR is not GPU-memory friendly (superlinear growth w.r.t. the number of points) and runs out of memory when the input point cloud reaches 80K points (note that we test PGR on an NVIDIA GeForce RTX 3090 graphics card with 24GB of GPU memory). In contrast, our method can deal with complicated geometry/topology and faithfully recover the normal vectors.

Real scans. Fig. 20 shows three raw point clouds, each of which is down-sampled to 10K points. From the color-coded visualization of normals, as well as the reconstructed surfaces, it can be seen that our method can effectively orient the normals for real-life objects, which validates the usefulness of our algorithm in practical scenarios.

5.6 Discussion on Global Methods

In the following, we make a discussion on the global methods including iPSR [Hou et al. 2022], PGR [Lin et al. 2022] and ours.

Ours v.s. iPSR. iPSR, as a global method, is excellent in estimating oriented normals. Benefiting from Poisson surface reconstruction, it



Fig. 21. Two parameter settings of PGR [Lin et al. 2022]. PGR_1: wmin=0.04, alpha=2.0. PGR_2: wmin=0.0015, alpha=1.05.

has many nice features. In its nature, iPSR gets more and more prior during the iterations of the reconstruction surface. If the given raw data does not have serious imperfections or challenging structures, iPSR can produce desirable normals, as well as a high-quality reconstruction surface. On the flip side, iPSR inherits some disadvantages of Poisson surface reconstruction. For example, iPSR cannot deal with the point clouds of an open surface, as shown in Fig. 17. Additionally, when the point clouds are as complex as Fig. 19, iPSR cannot reverse the false normals to the correct configuration and easily cause disconnection or adhesion, especially around thin structures. To summarize, the biggest weakness of iPSR lies in that if the initial surface is much different from the target surface, the structural/topological issues are hard to be fixed.

Ours v.s. PGR. First, in the original paper of PGR, the authors recommend several groups of parameters, depending on the number of points in the raw data. In contrast, our parameters remain the same for all the experiments, independent of the size of the raw data. Second, the statistics (available in the supplementary material) show that our method has better accuracy in predicting normals due to the alignment term that enforces the normals to point toward outside Voronoi poles, whereas, the inaccurate normals produced by PGR weaken the ability of fidelity preserving. Fig. 21 shows that the inaccurate normals of PGR cause a failure in recovering the center hole of the star shape, and any recommended parameters. Finally, PGR incurs a quadratic complexity of computational time and memory footprint, which limits its practical usage, especially on large models. For example, PGR fails to deal with the complex shapes shown in Fig. 19.

5.7 Run-time Performance

We provide the run-time performance statistics in Table 3. The tests are made on the torus model with different resolutions ranging from 0.5K points to 10K points. The total running time mainly consists of the construction of the Voronoi diagram and the optimization. It can be seen that optimization is the most time-consuming stage due to (1) the number of variables is twice as large as the number of the points, and (2) the objective function has to be evaluated by a double loop, i.e., over each \mathbf{p}_i and each \mathbf{q}_i , leading to a non-linear climbing in the computational overhead. But we must point out that even for the Torus model with 10K points, generally, 50 iterations, computed in 10 minutes, suffice to arrive at the termination. The overhead is acceptable for many non-real-time geometry processing tasks.

Table 3. Running time (in seconds) of different methods w.r.t. the number of points #V. We test with the Torus model.

#V	0.5K	1K	3K	5K	7K	10K
Норре	0.324	0.477	0.625	0.967	1.112	1.569
König	0.306	0.353	0.625	0.815	1.017	1.185
PCPNet	4.226	5.446	6.388	8.753	11.015	12.581
Dipole	3.277	3.565	5.489	8.411	11.602	14.517
PGR	0.228	0.260	0.489	0.612	0.823	1.020
iPSR	2.801	3.535	4.321	4.543	4.476	5.173
Ours	5.240	15.499	72.434	174.541	282.294	559.854

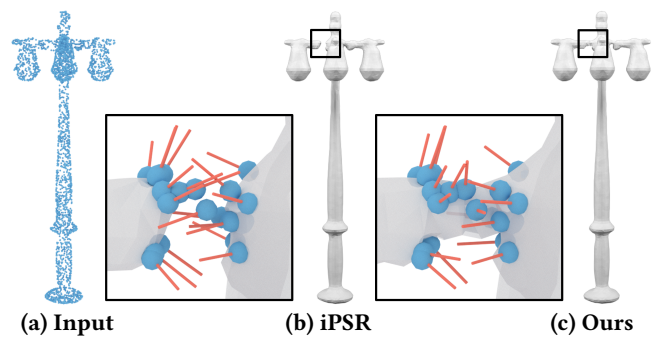


Fig. 22. We sample 3K points from the Lamp model ShapeNet [Chang et al. 2015]. Compared with iPSR [Hou et al. 2022], our method produces better reconstruction quality. However, the highlighted part shows that our predicted normals are not very accurate, leading to a conspicuous artifact in the reconstructed surface.

LIMITATIONS AND FUTURE WORK

The first limitation lies in the run-time performance. As we have to repeatedly evaluate the winding number for each data point and each query point, the timing cost spent in a single computation of the objective function amounts to O(NM), where N and M are respectively the number of data points and the number of query points. To alleviate this, one could downsample the input point set. After the normals of the subset are estimated, the un-oriented points can get normals by a simple propagation. Another direction of boosting the run-time performance is to develop a GPU version to further improve the parallelism.

The second limitation is that there is room for further improvement in the accuracy of predicted normals. In Fig. 22, we sample 3K points on the Lamp model from ShapeNet [Chang et al. 2015]. Our predicted normals are much different from the ground-truth normals, in spite of being better than iPSR [Hou et al. 2022]. The inaccurate normals lead to a conspicuous artifact in the reconstructed surface. In the future, we shall further improve the prediction accuracy based on prior knowledge about the geometry/topology.

Finally, our method may fail when there are many points scattered inside the volume, or a high-density point cloud is coupled with highlevel noise. Both situations may violate the 0−1 balance requirement, potentially resulting in a failure case. To address these challenges, it is necessary to develop some pre-processing techniques to filter out those points that do not contribute to the underlying surface at all.

7 CONCLUSION

This paper presents a globally consistent normal orientation method by regularizing the winding-number field. We formulate the normal orientation problem into an optimization-driven framework that considers three requirements in the objective function, two of which specify requirements on the winding-number field and the other term constraining the alignment with Voronoi poles. We conduct extensive experiments on point clouds with various imperfections and challenges, such as noise, data sparsity, nearby gaps, thin-walled plates, and highly complex geometry/topology. Experimental results exhibit the advantage of the proposed approach.

ACKNOWLEDGMENTS

The authors would like to thank the anonymous reviewers for their valuable comments and suggestions. This work is supported by the National Key R&D Program of China (2021YFB1715900), the National Natural Science Foundation of China (62002190, 62272277, 62072284), and the Natural Science Foundation of Shandong Province (ZR2020MF036, ZR2020MF153). Ningna Wang and Xiaohu Guo were partially supported by National Science Foundation (OAC-2007661).

APPENDIX

A f HAS A LOWER BOUND

In order to show that the minimization of $f(\mathbf{n})$ (see Eq. (2) in the paper) can arrive at the termination, we need to prove why the objective function has a lower bound.

Recall that $f(\mathbf{n})$ has three terms f_{01} , f_A and f_B . By assuming that the maximum of $\|\mathbf{q}_k^i - \mathbf{p}_i\|$ is L, the diagonal length of the enclosing box, we have

$$|f_{A}(\mathbf{n})| \leq \sum_{i}^{N} \left| \frac{1}{M_{i}} \sum_{k}^{M_{i}} w_{k}^{i} \mathbf{n}_{i} \cdot (\mathbf{q}_{k}^{i} - \mathbf{p}_{i}) \right|$$

$$\leq \sum_{i}^{N} \left(\frac{L}{M_{i}} \sum_{k}^{M_{i}} |w_{k}^{i}| \right).$$
(8)

Therefore, it is easy to show that f_{01} is quartic about w_j while f_A and f_B can be bounded by a lower-degree polynomial function about w_j . Suppose that w_j goes to $+\infty$ or $-\infty$. f_{01} must approach $+\infty$ in either case. Considering that f_{01} has a higher rate of change than f_A and f_B , we can conclude that when w_j goes to $+\infty$ or $-\infty$, the overall value of $f(\mathbf{n})$ must approach $+\infty$. As our goal is to minimize $f(\mathbf{n})$, w_j must be naturally constrained to a limited range of $[W_1, W_2]$. The boundedness of $f(\mathbf{n})$ can be immediately verified based on the fact that $f(\mathbf{n})$ is a continuous function in the closed interval $[W_1, W_2]$.

B MORE COMPARISON

Angle RMSE. In the main paper, we give the statistics about the ratio of true normals. Here we further give the statistics about the Root Mean Square Error (RMSE) of the angles between the estimated normals and the ground truth normals.

Normal Evaluation Using Angle RMSE. In Sec. 5.4, we give a visual comparison to exhibit the noise-resistant ability of our approach compared with the SOTA methods [Guerrero et al. 2018; Hoppe et al. 1992; König and Gumhold 2009; Lin et al. 2022; Metzer et al.

2021]. We report the angle RMSE statistics under four different sampling conditions in Table 4. It can be clearly seen that our method surpasses the other methods in terms of normal orientations. Even if the noise level amounts to 0.5%, our method can still get the best score for 55% of the models, and a competitive score for another 40%. For example, the best score (10.336) is given by Hoppe on the Knot model, and ours is the second best (17.086), which is much better than the remaining scores 44.105, 71.110 and 93.984.

There are some methods such as PCA [Rusu and Cousins 2011], AdaFit [Zhu et al. 2021] and NeAF [Li et al. 2022] that focus on normal estimation. We also include them for comparison; See the statistics in Table 5. The statistics show that our algorithm has a big advantage of prediction accuracy over the SOTA methods, on all the 18 models and under all the 4 noise sampling conditions.

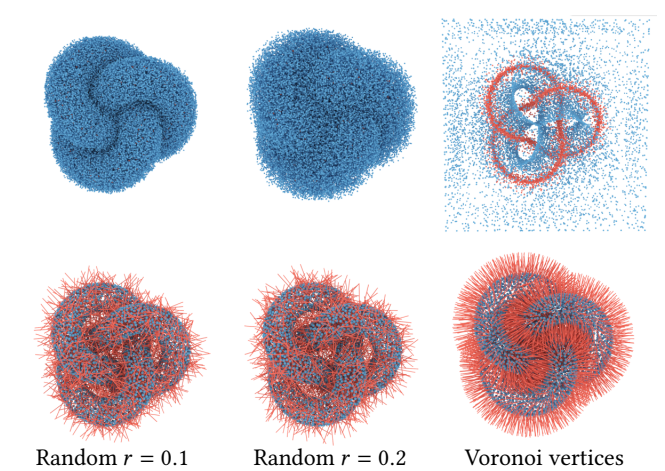


Fig. 23. In order to test different sampling strategies, we generate Gaussian noise near the point cloud (radius $r=0.1~{\rm or}~0.2$) to produce examination points. First column: r=0.1 (top: examination points; bottom: normals). Second column: r=0.2 (top: examination points; bottom: normals). Last column: Voronoi vertices as examination points. It can be seen that Voronoi vertices are more suitable for serving as the examination points. Note that we iterate 200 steps for r=0.1,0.2 and 40 steps for the situation of Voronoi vertices as examination points.

C STRATEGIES FOR GENERATING EXAMINATION POINTS

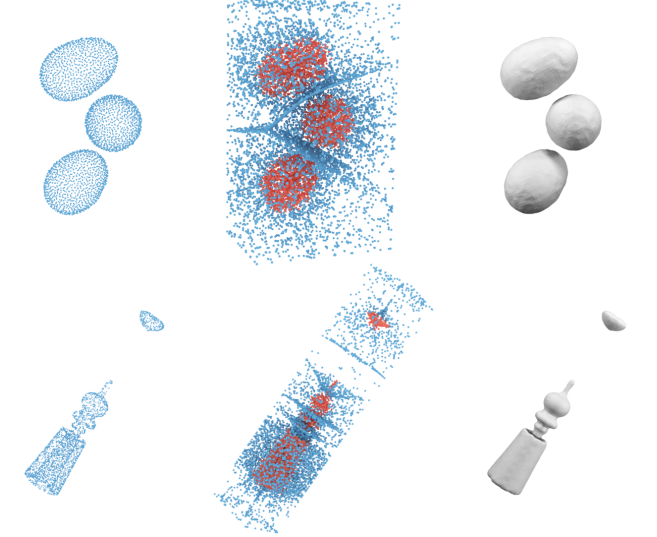
We conduct the ablation study about different strategies for generating examination points. Specially, we compare our Voronoi-based sampling strategy with the off-surface random sampling strategy. As shown in Fig. 23, we randomly sample points around the surface of the shape with two sampling radii r=0.1 and r=0.2. Note that we iterate 200 steps for r=0.1,0.2 and 40 steps for the situation of Voronoi vertices as examination points. It can be seen that Voronoi vertices are more suitable for serving as the examination points. The superiority of Voronoi-based sampling is due to the fact that the majority of Voronoi vertices are located either deepest inside the surface, or furthest outside the surface (approximating the inner and outer medial axis [Amenta et al. 2001]). Thus their distribution of winding numbers is more likely to be pushed towards 0 and 1, compared with the random sampling strategy.

Sampling Blue Noise Sampling White Noise Sampling White Noise Sampling With 0.25% noise White Noise Sampling With 0.5% noise Models PCPNet Dipole Hoppe PCPNet Dipole PCPNet Dipole König PCPNet Dipole PGR Ours König Hopp 82-block 117.870 52.218 24.837 18.631 22.972 36.191 19.890 58 451 22.205 27.425 77.330 27.192 23.581 9.324 28.607 84.449 48.111 34.774 77.731 45.505 60.557 bunny chair 96.834 cup-22 18.583 107.427 88.692 109.907 17.573 9.227 103.229 103.407 89.561 107.211 24.954 13.710 44.816 104.835 90.176 106.561 48,635 14.220 109.334 103,585 90.580 104.788 69.075 20.870 89 978 67 295 120 922 19 711 15 208 108 913 112 636 21 614 17 309 67 185 114 834 49 497 21 296 106 810 113 894 19 041 19.243 5.428 31.515 42.304 25.464 6.225 21.070 **6.225** 37.061 42.841 63.276 55.063 24.943 21.032 37.920 44.039 63.270 52.910 53.196 59.078 27.474 7.836 40.835 39.086 52.236 76.762 83.886 22.594 24.310 10.283 holes 5.428 21.160 6.667 horse 33.319 31.786 46.661 24.270 23.428 36.567 37.052 49.740 22.636 17.222 45.777 50.092 39.566 44.637 66.504 21.637 42.982 51.202 41.717 53.306 88.838 39.494 16.164 9.882 36.495 28.360 18.149 12.834 13.994 11.001 43.810 25,569 19.388 12.335 13,970 11.249 44.775 24.671 59.984 14.473 14.873 11.980 45.921 27.288 80.554 31.773 47.223 21.448 5.291 **32.986** 29.550 8.174 42.277 27.995 116.168 55.818 118.247 7.929 46.637 102.424 93.984 59.108 117.068 87.369 55.493 6.838 52.103 6.121 23.621 57.246 75.879 10.336 59.319 44.105 50.398 4.634 6.012 71.819 95,297 10.086 77 715 40.831 49.633 mobius 26.234 122.025 53.639 120.832 121.133 55.871 26.797 28.346 120.963 61.251 117.930 60.265 119.506 120.518 73.098 88.530 99.870 78.598 94.666 20.618 27.405 9.458 22.274 99.145 77.615 11.399 22.743 97.616 77.761 93.732 47.326 12.412 95.910 96.303 77.940 95.133 17.144 115.579 63.804 21.108 31.533 30.227 115.992 60.782 27.439 41.275 28,288 42.195 112.586 105.038 30.186 41.486 56.832 62.286 35.594 40.633 80.510 121.682 3.239 117.485 19.187 119.934 3.723 119.905 3.723 110.042 5.376 35.829 16.290 7.455 23.038 4.167 119.754 4.167 109.920 4.775 43.734 61.542 48.894 119.582 5.510 119.680 **5.510** 73.599 38.420 32.310 19.166 sheet 3.239 17.275 trim-star 24.069 18.808 48.281 43.216 29.519 17.774 34.325 51.527 31.829 25.209 20.848 52.233 61.031 26.540 21.339 53.525 81.154 48.036 59.083 21.234 13.957 52.584 41.840 53.557 69.580 61.422 52.113 29.463

Table 4. Comparison of the angle RMSE with the SOTA methods at different sampling conditions.

Table 5. Comparison of normal orientation with three normal estimation methods.

Sampling		Blue Nois	se Sampli	ng	White Noise Sampling				0.25% noise White Noise Sampling				0.5% noise White Noise Sampling			
Models	PCA	AdaFit	NeAF	Ours	PCA	AdaFit	NeAF	Ours	PCA	AdaFit	NeAF	Ours	PCA	AdaFit	NeAF	Ours
82-block	75.950	50.150	51.800	100.000	75.675	50.675	51.225	99.980	75.625	51.225	52.250	99.930	75.825	52.050	53.650	99.880
bunny	89.750	51.375	50.375	100.000	89.800	51.375	50.125	99.750	89.725	50.475	50.300	99.980	89.775	50.850	50.800	99.580
chair	62.775	53.125	50.625	100.000	64.250	52.750	50.100	100.000	63.575	52.825	54.000	100.000	64.825	52.125	51.050	99.400
cup-22	58.425	52.225	52.000	100.000	58.175	50.075	51.550	99.950	58.550	50.150	51.325	99.950	58.450	50.550	50.175	99.850
cup-35	66.775	50.775	51.550	100.000	67.725	50.525	50.350	100.000	68.025	50.200	52.250	100.000	67.600	51.450	53.650	100.000
fandisk	90.200	54.950	50.700	100.000	90.000	55.075	50.975	100.000	90.050	54.675	50.675	99.950	89.975	54.775	51.650	99.750
holes	79.275	50.575	51.325	100.000	79.350	51.200	51.175	100.000	79.650	51.575	50.675	100.000	79.075	50.900	51.650	100.000
horse	81.875	50.200	50.600	99.500	80.275	51.050	50.500	99.800	80.800	50.350	51.800	99.750	80.625	51.350	51.025	97.500
kitten	90.977	55.011	51.937	100.000	91.075	57.325	51.750	99.980	90.975	57.625	53.875	100.000	90.950	57.100	51.250	99.980
knot	72.975	50.100	51.050	100.000	72.750	50.825	50.250	100.000	72.875	50.925	52.100	100.000	72.275	50.775	51.850	99.980
lion	85.275	53.025	52.125	99.380	84.900	54.575	50.275	99.700	85.200	54.750	52.625	99.550	85.475	55.775	51.850	93.830
mobius	55.225	53.700	53.050	100.000	55.425	54.575	54.625	100.000	55.500	53.800	52.500	97.380	54.875	53.825	52.650	85.780
mug	64.775	50.575	53.525	100.000	67.250	50.650	50.875	100.000	67.225	50.825	52.125	100.000	66.825	51.000	52.950	100.000
octa-flower	98.800	50.275	51.750	100.000	94.750	51.550	53.050	99.330	94.650	51.525	50.900	98.800	94.775	51.700	51.800	98.550
sheet	83.600	54.425	56.400	100.000	71.575	51.925	51.625	100.000	71.750	51.550	51.775	99.950	71.325	51.775	52.000	98.980
torus	89.225	50.125	53.800	100.000	89.950	50.500	52.100	100.000	89.950	50.350	51.000	100.000	90.125	50.225	50.400	100.000
trimstar	80.975	50.300	52.625	100.000	81.150	50.325	53.475	100.000	81.125	51.250	50.750	100.000	81.250	51.375	51.175	100.000
vase	84.575	53.400	50.375	100.000	86.350	51.825	50.250	100.000	86.725	52.050	51.475	100.000	86.275	52.500	50.450	99.650



(a) Input points (b) Voronoi vertices (c) Reconstruction

Fig. 24. Our method can handle multiple disconnected components and outliers. In the middle column, the interior Voronoi vertices (whose winding number is close to 1) are colored in red while the exterior Voronoi vertices (whose winding number is close to 0) are colored in blue.

DISCONNECTED COMPONENTS AND OUTLIERS

In this section, we show that our method can also handle multiple disconnected components and outliers. In the top row of Fig. 24, our Voronoi-based sampling method can still distinguish the interior Voronoi vertices (whose winding number is close to 1) and the exterior Voronoi vertices (whose winding number is close to 0). At the same time, in the bottom row of Fig. 24, we show an outlier example where the cap is completely away from the main body. It can be clearly seen that our approach can deal with outliers as well. On one hand, the Voronoi diagram can capture the proximity between data points, thus encouraging the outlier points to be oriented independently of the main body. Additionally, the winding number field helps infer normal consistency from a global perspective, thus unlikely to suffer from small imperfections.

WIND-NUMBER FIELD UNDER DIFFERENT **CONDITIONS**

We show more winding-number fields in Fig. 25. Despite the varying topologies, all the winding-number fields are approximately binaryvalued at 1 and 0. Moreover, we visualize how the winding-number field distribution changes with respect to the sampling density in Fig. 26. It can be seen that the winding-number field remains binaryvalued with approximate values of 1 and 0 as the number of points increases from 1K to 10K.

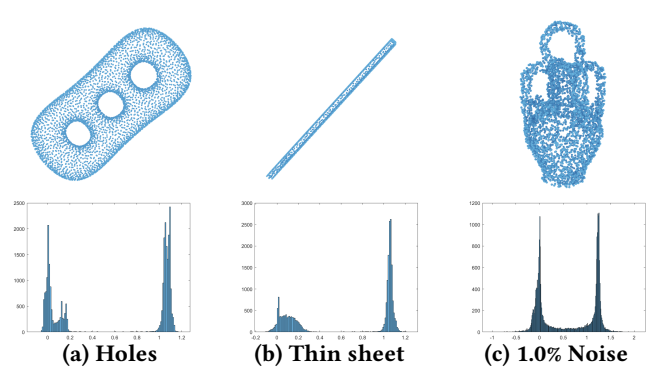


Fig. 25. The winding-number field distributions on three totally different shapes.

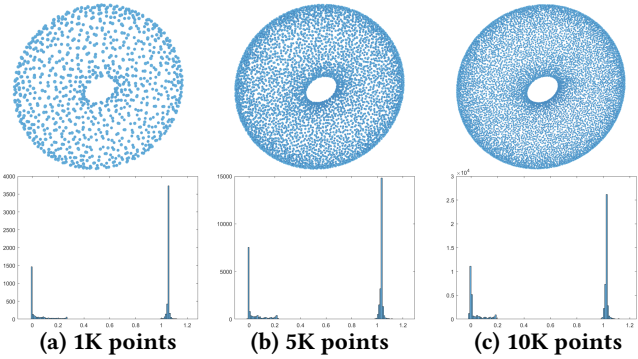


Fig. 26. The winding-number field distributions under different sampling densities.

F ABLATION STUDY

 λ_A and λ_B . We first investigate the influence of the coefficients λ_A and λ_B in Eq. (2). We test different combinations of λ_A and λ_B in Fig. 27. The quantitative statistics are summarized in Table 6. We have two observations:

- (1) If λ_B is too small, the winding numbers at the vertices of a Voronoi cell may not be balanced, all staying at 0 or 1. But if λ_B is too large, our algorithm may report a reverse orientation for a small point patch.
- (2) If λ_A is too small, the predicted normal orientations are not accurate (see Table 6). Instead, if λ_A is too large, it may prevent the orientations from evolving to a favorite state.

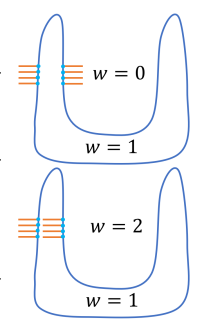
As $\lambda_A=10, \lambda_B=50$ gets the best scores in Table 6, we select $\lambda_A=10, \lambda_B=50$ as the favorite combination, which is used in all the experiments in this paper.

Optimization Terms. We conduct the ablation study about the constituent terms in Eq. (2). From the top row of Fig. 28, we have the following observations:

(1) The term f_{01} enforces the winding number to be valued at 0 or 1. Without f_{01} , the global normal consistency cannot be guaranteed. Two points on the opposite sides of the thin wall may be different from the ground-truth orientations.

- (2) The term f_A is to enforce the normals to align with Voronoi poles. Without f_A , the orientations remain nearly unchanged but the accuracy is decreased; See the statistics in Table 7.
- (3) The term f_B is to eliminate the occurrence that all the vertices of a Voronoi cell are inside or outside. Without f_B , the normals tend to stay at the initial random state; the winding number is 0 almost everywhere.

Furthermore, the double well function is very helpful for regularizing the winding number. If we replace the double well function with a single well function $y=(x-1)^2$ (see the left bottom result of Fig. 28), it will confuse 0 and 2 in inferring the winding-number values, as the effects of 0 and 2 are exactly the same; See the inset figure. Besides, the shear correction term $\frac{w_j}{D}$ is also helpful for preventing the normal setting from staying in the initial random state and pushing



the winding number of some examination points to approach 1.

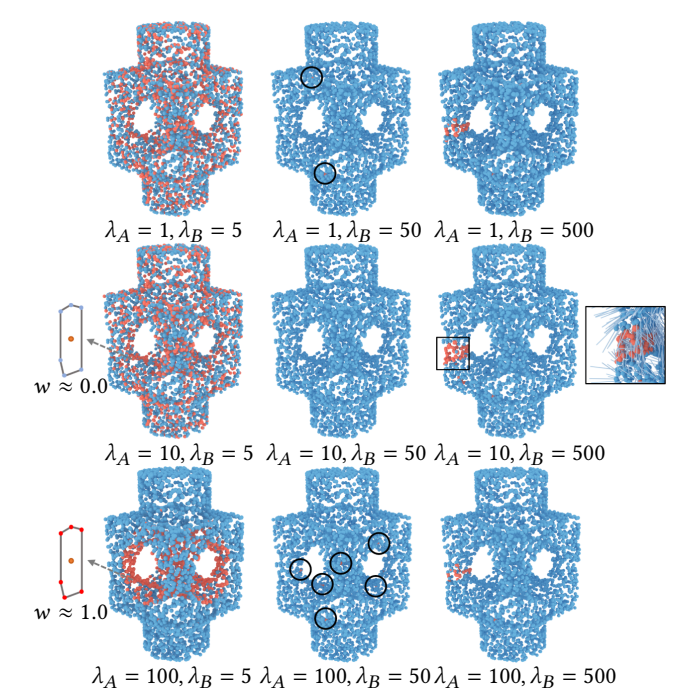


Fig. 27. Ablation study about the weighting coefficients λ_B and λ_A . We select $\lambda_A=10, \lambda_B=50$ as the favorite combinations, which are used in all the experiments in this paper. If λ_B is too small (see the left column), the winding numbers at the vertices of a Voronoi cell may all stay at 0 or 1. The predicted orientation is true if the angle between the computed normal and the ground-truth normal is less than 90 degrees. We colored the true predictions and false predictions in blue and red, respectively.

Besides, we conduct an ablation study about different strategies for generating examination points. By comparing our Voronoi-based sampling strategy with the off-surface random sampling strategy, we validate the superiority of Voronoi-based sampling. The majority of Voronoi vertices are located either deepest inside the surface or furthest outside the surface (the same reason that *power crust* [Amenta

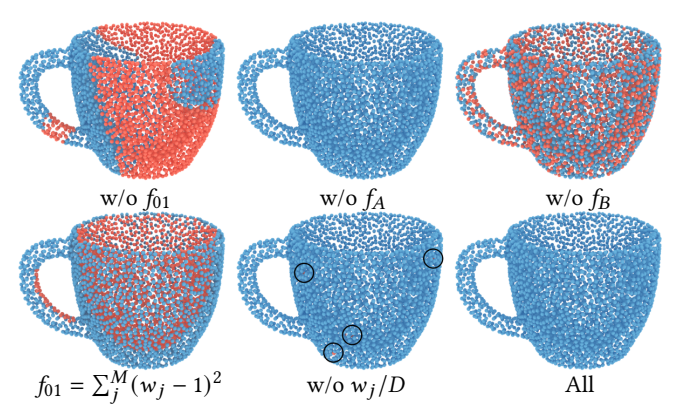


Fig. 28. Ablation study about the constituent terms in Eq. (2). Note that the bottom left figure shows the result when we replace the double well function with a single well function $y = (x - 1)^2$.

Table 6. Quantitative results of normal orientation with different weighting schemes. Indicators are described in Sec. 5.2.

Parameters	RMSE ↓	Ratio _{truth} ↑	$CD_{recon} \downarrow$
$\lambda_A = 1, \lambda_B = 5$	95.797	63.600	1.899
$\lambda_A = 1, \lambda_B = 50$	21.117	99.875	0.141
$\lambda_A = 1, \lambda_B = 500$	26.039	99.050	0.177
$\lambda_A = 10, \lambda_B = 5$	95.501	63.925	0.187
$\lambda_A = 10, \lambda_B = 50$	19.901	99.975	0.139
$\lambda_A = 10, \lambda_B = 500$	29.979	98.225	0.198
$\lambda_A = 100, \lambda_B = 5$	73.566	80.600	0.749
$\lambda_A = 100, \lambda_B = 50$	23.484	99.450	0.142
$\lambda_A = 100, \lambda_B = 500$	24.897	99.275	0.172

et al. 2001] used them as candidates for the medial axis). Thus their distribution of winding numbers is more likely to be pushed towards 0 and 1, compared with the random sampling strategy.

Table 7. Quantitative results of normal orientation using different terms in Eq. (2). Indicators are described in Sec. 5.2.

Terms	RMSE ↓	$Ratio_{\mathrm{truth}} \uparrow$	$CD_{recon} \downarrow$
w/o f ₀₁	106.162	54.700	1.753
w/o f_A	13.810	100.000	0.069
w/o f_B	98.908	57.600	2.160
$f_{01} = \sum_{j}^{M} (w_j - 1)^2$	110.814	59.150	1.920
$w/o w_j/D$	17.556	99.850	0.094
All	10.632	100.000	0.067

THE INFLUENCE OF INITIALIZATION STRATEGIES

As shown in Figure 29, our method exhibits high robustness across different initialization strategies, as demonstrated through three strategies: (1) reversed normal initialization, (2) random initialization, and (3) initialization using PCPNet [Guerrero et al. 2018]. Our method achieves more accurate normal orientation results for any of the initialization strategies. An interesting observation is that our method requires much less computational cost if initialized by PCP-Net [Guerrero et al. 2018]. Note that the stop criteria for the three strategies are the same, i.e., when the difference of the objective value between two successive iterations are small enough.

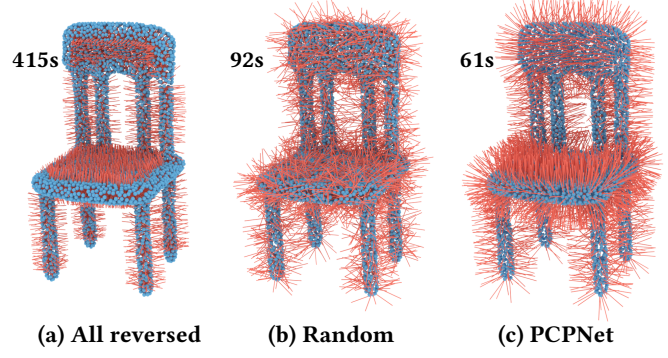


Fig. 29. Normal orientation results using different initialization strategies: (a) all reversed normal initialization, (b) random initialization, and (c) initialization by PCPNet [Guerrero et al. 2018]. Their timings are 415s, 92s, and 61s, respectively.

GRADIENT FUNCTION

Herein, we provide the gradient of our objective function. Note we parameterize each normal vector \mathbf{n}_i with (u_i, v_i) .

$$\mathbf{n}_i = (\sin(u_i)\cos(v_i), \sin(u_i)\sin(v_i), \cos(u_i)) \tag{9}$$

We start by deriving the gradient of winding-number field w(q)w.r.t. u_i and v_i . Let $L = (p_i - q)$, then we have:

$$\frac{\partial w(q)}{\partial v_i} = \frac{a_i L \cdot n_i}{4\pi \left\| L \right\|^3} \left(-L_x sin(u_i) sin(v_i) + L_y sin(u_i) cos(v_i) \right) \tag{10}$$

$$\frac{\partial w(q)}{\partial u_i} = \frac{a_i L \cdot n_i}{4\pi \left\| L \right\|^3} (L_x cos(u_i) cos(v_i) + L_y cos(u_i) sin(v_i) - L_z sin(u_i))$$

Similarly, the gradient of each objective term w.r.t. u_i and v_i is given as follows

$$f'_{01}(u_i) = \sum_{i=1}^{M} \left(\frac{4}{\sqrt{\sigma}} \left(\frac{w_j - c}{\sqrt{\sigma}}\right)^3 - \frac{2}{\sqrt{\sigma}} \left(\frac{w_j - c}{\sqrt{\sigma}}\right) - \frac{1}{D}\right) \frac{\partial w_j}{\partial u_i}$$
(11)

$$f'_{01}(v_i) = \sum_{j=1}^{M} \left(\frac{4}{\sqrt{\sigma}} \left(\frac{w_j - c}{\sqrt{\sigma}}\right)^3 - \frac{2}{\sqrt{\sigma}} \left(\frac{w_j - c}{\sqrt{\sigma}}\right) - \frac{1}{D}\right) \frac{\partial w_j}{\partial v_i}$$
(12)

$$f_B'(u_i) = -\sum_{j}^{N} \sum_{k}^{M_i} \frac{2\left\| w_k^j - \bar{w}^j \right\|}{M_j} \left(\frac{\partial w_k^j}{\partial u_i} - \sum_{k}^{M_j} \frac{1}{M_j} \frac{\partial w_k^j}{\partial u_i} \right)$$
(13)

$$f_B'(v_i) = -\sum_{j}^{N} \sum_{k}^{M_i} \frac{2\left\| w_k^j - \bar{w}^j \right\|}{M_j} \left(\frac{\partial w_k^j}{\partial u_i} - \sum_{k}^{M_j} \frac{1}{M_j} \frac{\partial w_k^j}{\partial v_i} \right)$$
(14)

$$f'_{A}(u_{i}) = \sum_{j}^{N} \sum_{k}^{M_{i}} \frac{-(n_{j} \cdot (q_{k}^{j} - p_{j}))}{M_{j}} \frac{\partial w_{j}}{\partial u_{i}}$$

$$+ \sum_{k}^{M_{i}} \frac{-(L_{x}cos(u_{i})cos(v_{i}) + L_{y}cos(u_{i})sin(v_{i}) - L_{z}sin(u_{i}))w_{k}^{i}}{M_{i}}$$
(15)

$$f_A'(v_i) = \sum_{j}^{N} \sum_{k}^{M_i} \frac{-(n_j \cdot (q_k^j - p_j))}{M_j} \frac{\partial w_j}{\partial v_i}$$

$$+ \sum_{k}^{M_i} \frac{(L_x sin(u_i) sin(v_i) - L_y sin(u_i) cos(v_i)) w_k^i}{M_i}$$

$$(16)$$

REFERENCES

- Pierre Alliez, David Cohen-Steiner, Yiying Tong, and Mathieu Desbrun. 2007. Voronoi-based variational reconstruction of unoriented point sets. In *Proc. of Symp. of Geometry Processing*, Vol. 7. 39–48.
- Nina Amenta and Marshall Bern. 1998. Surface reconstruction by Voronoi filtering. In Proceedings of the fourteenth annual symposium on Computational geometry. 39–48.
- Nina Amenta, Sunghee Choi, and Ravi Krishna Kolluri. 2001. The power crust. In Proceedings of the sixth ACM symposium on Solid modeling and applications. 249–
- Samir Aroudj, Patrick Seemann, Fabian Langguth, Stefan Guthe, and Michael Goesele. 2017. Visibility-consistent thin surface reconstruction using multi-scale kernels. ACM Trans. on Graphics 36, 6 (2017), 1–13.
- Haim Avron, Andrei Sharf, Chen Greif, and Daniel Cohen-Or. 2010. 11-sparse reconstruction of sharp point set surfaces. ACM Trans. on Graphics 29, 5 (2010), 1–12.
- Gavin Barill, Neil G Dickson, Ryan Schmidt, David IW Levin, and Alec Jacobson. 2018. Fast winding numbers for soups and clouds. *ACM Trans. on Graphics* 37, 4 (2018), 1–12
- Yizhak Ben-Shabat and Stephen Gould. 2020. Deepfit: 3d surface fitting via neural network weighted least squares. In ECCV. Springer, 20–34.
- Yizhak Ben-Shabat, Michael Lindenbaum, and Anath Fischer. 2019. Nesti-net: Normal estimation for unstructured 3d point clouds using convolutional neural networks. In IEEE CVPR. 10112–10120.
- Dobrina Boltcheva and Bruno Lévy. 2017. Surface reconstruction by computing restricted Voronoi cells in parallel. Computer-Aided Design 90 (2017), 123–134.
- Frédéric Cazals and Marc Pouget. 2005. Estimating differential quantities using polynomial fitting of osculating jets. Comp. Aided Geom. Design 22, 2 (2005), 121–146.
- Angel X Chang, Thomas Funkhouser, Leonidas Guibas, Pat Hanrahan, Qixing Huang, Zimo Li, Silvio Savarese, Manolis Savva, Shuran Song, Hao Su, et al. 2015. Shapenet: An information-rich 3d model repository. arXiv preprint arXiv:1512.03012 (2015).
- Cheng Chi and Shuran Song. 2021. GarmentNets: Category-Level Pose Estimation for Garments via Canonical Space Shape Completion. In IEEE ICCV. 3324–3333.
- Tamal K Dey and Samrat Goswami. 2004. Provable surface reconstruction from noisy samples. In Proceedings of the twentieth annual symposium on Computational Geometry. 330–339.
- Tamal K Dey, Gang Li, and Jian Sun. 2005. Normal estimation for point clouds: A comparison study for a Voronoi based method. In Proceedings Eurographics/IEEE VGTC Symposium Point-Based Graphics, 2005. IEEE, 39–46.
- Zhiyang Dou, Cheng Lin, Rui Xu, Lei Yang, Shiqing Xin, Taku Komura, and Wenping Wang. 2022. Coverage Axis: Inner Point Selection for 3D Shape Skeletonization. In Computer Graphics Forum, Vol. 41. Wiley Online Library, 419–432.
- Eleonora Grilli, Fabio Menna, and Fabio Remondino. 2017. A review of point clouds segmentation and classification algorithms. The International Archives of Photogrammetry, Remote Sensing and Spatial Information Sciences 42 (2017), 339.
- Cindy Grimm and William D Smart. 2011. Shape classification and normal estimation for non-uniformly sampled, noisy point data. Computers & Graphics 35, 4 (2011), 904–915
- Paul Guerrero, Yanir Kleiman, Maks Ovsjanikov, and Niloy J Mitra. 2018. Pcpnet learning local shape properties from raw point clouds. In Computer Graphics Forum, Vol. 37. Wiley Online Library, 75–85.
- Godfrey Harold Hardy, John Edensor Littlewood, George Pólya, György Pólya, et al. 1952. *Inequalities*. Cambridge university press.
- Taisuke Hashimoto and Masaki Saito. 2019. Normal Estimation for Accurate 3D Mesh Reconstruction with Point Cloud Model Incorporating Spatial Structure.. In CVPR workshops, Vol. 1.
- Hugues Hoppe, Tony DeRose, Tom Duchamp, John McDonald, and Werner Stuetzle. 1992. Surface reconstruction from unorganized points. In *Proc. ACM SIGGRAPH*. 71–78.
- Fei Hou, Chiyu Wang, Wencheng Wang, Hong Qin, Chen Qian, and Ying He. 2022. Iterative Poisson surface reconstruction (iPSR) for unoriented points. ACM Trans. on Graphics (Proc. SIGGRAPH) (2022).
- Yixin Hu, Teseo Schneider, Bolun Wang, Denis Zorin, and Daniele Panozzo. 2020. Fast tetrahedral meshing in the wild. ACM Transactions on Graphics (TOG) 39, 4 (2020), 117–1.
- Yixin Hu, Qingnan Zhou, Xifeng Gao, Alec Jacobson, Denis Zorin, and Daniele Panozzo. 2018. Tetrahedral Meshing in the Wild. *ACM Trans. on Graphics* (2018).

- Zhiyang Huang, Nathan Carr, and Tao Ju. 2019. Variational implicit point set surfaces. ACM Transactions on Graphics (TOG) 38, 4 (2019), 1–13.
- Zhangjin Huang, Yuxin Wen, Zihao Wang, Jinjuan Ren, and Kui Jia. 2022. Surface Reconstruction from Point Clouds: A Survey and a Benchmark. arXiv preprint arXiv:2205.02413 (2022).
- Alec Jacobson et al. 2021. gptoolbox: Geometry Processing Toolbox. http://github.com/alecjacobson/gptoolbox.
- Alec Jacobson, Ladislav Kavan, and Olga Sorkine-Hornung. 2013. Robust inside-outside segmentation using generalized winding numbers. ACM Trans. on Graphics 32, 4 (2013). 1–12.
- Johannes Jakob, Christoph Buchenau, and Michael Guthe. 2019. Parallel globally consistent normal orientation of raw unorganized point clouds. In Computer Graphics Forum, Vol. 38. Wiley Online Library, 163–173.
- V Jelic and F Marsiglio. 2012. The double-well potential in quantum mechanics: a simple, numerically exact formulation. European Journal of Physics 33, 6 (2012), 1651
- Michael Kazhdan. 2005. Reconstruction of solid models from oriented point sets. In Eurographics Symposium on Geometry Processing. 73–es.
- Michael Kazhdan, Matthew Bolitho, and Hugues Hoppe. 2006. Poisson surface reconstruction. In Eurographics Symposium on Geometry Processing, Vol. 7.
- Michael Kazhdan and Hugues Hoppe. 2013. Screened poisson surface reconstruction. ACM Trans. on Graphics 32, 3 (2013), 1–13.
- Ravikrishna Kolluri, Jonathan Richard Shewchuk, and James F O'Brien. 2004. Spectral surface reconstruction from noisy point clouds. In Proceedings of the 2004 Eurographics/ACM SIGGRAPH symposium on Geometry processing. 11–21.
- Sören König and Stefan Gumhold. 2009. Consistent Propagation of Normal Orientations in Point Clouds. In VMV. 83–92.
- Jan Eric Lenssen, Christian Osendorfer, and Jonathan Masci. 2020. Deep iterative surface normal estimation. In IEEE CVPR. 11247–11256.
- David Levin. 1998. The approximation power of moving least-squares. Mathematics of computation 67, 224 (1998), 1517–1531.
- David Levin. 2004. Mesh-independent surface interpolation. In Geometric modeling for scientific visualization. Springer, 37–49.
- Bao Li, Ruwen Schnabel, Reinhard Klein, Zhiquan Cheng, Gang Dang, and Shiyao Jin. 2010. Robust normal estimation for point clouds with sharp features. *Computers & Graphics* 34, 2 (2010), 94–106.
- Shujuan Li, Junsheng Zhou, Baorui Ma, Yu-Shen Liu, and Zhizhong Han. 2022. NeAF: Learning Neural Angle Fields for Point Normal Estimation. arXiv preprint arXiv:2211.16869 (2022).
- Siyou Lin, Dong Xiao, Zuoqiang Shi, and Bin Wang. 2022. Surface Reconstruction from Point Clouds without Normals by Parametrizing the Gauss Formula. *ACM Trans. on Graphics* 42, 2 (2022), 19 pages. https://doi.org/10.1145/3554730
- Xiuping Liu, Jie Zhang, Junjie Cao, Bo Li, and Ligang Liu. 2015. Quality point cloud normal estimation by guided least squares representation. Computers & Graphics 51 (2015) 106–116.
- Albrecht Ludwig Friedrich Meister. 1769. Generalia de genesi figurarum planarum et inde pendentibus earum affectionibus.
- Quentin Mérigot, Maks Ovsjanikov, and Leonidas J Guibas. 2010. Voronoi-based curvature and feature estimation from point clouds. IEEE Trans. on Vis. and Comp. Graphics 17, 6 (2010), 743–756.
- Gal Metzer, Rana Hanocka, Denis Zorin, Raja Giryes, Daniele Panozzo, and Daniel Cohen-Or. 2021. Orienting Point Clouds with Dipole Propagation. ACM Trans. on Graphics 40, 4, Article 165 (jul 2021), 14 pages. https://doi.org/10.1145/3450626. 3459835
- Niloy J Mitra and An Nguyen. 2003. Estimating surface normals in noisy point cloud data.

 In special issue of International Journal of Computational Geometry and Applications.
 322–328
- Stefano Nuvoli, Nico Pietroni, Paolo Cignoni, Riccardo Scateni, and Marco Tarini. 2022. SkinMixer: Blending 3D Animated Models. ACM Transactions on Graphics (TOG) 41, 6 (2022), 1–15.
- Daoshan OuYang and Hsi-Yung Feng. 2005. On the normal vector estimation for point cloud data from smooth surfaces. *Computer-Aided Design* 37, 10 (2005), 1071–1079. Mark Pauly, Richard Keiser, Leif P Kobbelt, and Markus Gross. 2003. Shape modeling
- with point-sampled geometry. ACM Trans. on Graphics 22, 3 (2003), 641–650. François Pomerleau, Francis Colas, Roland Siegwart, et al. 2015. A review of point cloud
- registration algorithms for mobile robotics. Foundations and Trends® in Robotics 4, 1 (2015), 1–104.
- Radu Bogdan Rusu and Steve Cousins. 2011. 3D is here: Point Cloud Library (PCL). In IEEE International Conference on Robotics and Automation (ICRA). IEEE.
- Silvia Sellán, Noam Aigerman, and Alec Jacobson. 2021. Swept volumes via spacetime numerical continuation. ACM Transactions on Graphics (TOG) 40, 4 (2021), 1–11.
- Silvia Sellán and Alec Jacobson. 2022. Stochastic Poisson Surface Reconstruction. ACM Transactions on Graphics (TOG) 41, 6 (2022), 1–12.
- Yujing Sun, Scott Schaefer, and Wenping Wang. 2015. Denoising point sets via L0 minimization. Comp. Aided Geom. Design 35 (2015), 2–15.

- Jun Wang, Zhouwang Yang, and Falai Chen. 2012. A variational model for normal computation of point clouds. The Visual Computer 28, 2 (2012), 163-174.
- Ningna Wang, Bin Wang, Wenping Wang, and Xiaohu Guo. 2022a. Computing Medial Axis Transform with Feature Preservation via Restricted Power Diagram. ACM Transactions on Graphics (TOG) 41, 6 (2022), 1-18.
- Pengfei Wang, Zixiong Wang, Shiqing Xin, Xifeng Gao, Wenping Wang, and Changhe Tu. 2022b. Restricted Delaunay Triangulation for Explicit Surface Reconstruction. ACM Transactions on Graphics (TOG) (2022).
- Zixiong Wang, Pengfei Wang, Qiujie Dong, Junjie Gao, Shuangmin Chen, Shiqing Xin, and Changhe Tu. 2021. Neural-IMLS: Learning Implicit Moving Least-Squares for Surface Reconstruction from Unoriented Point clouds. arXiv preprint arXiv:2109.04398 (2021).
- Hui Xie, Kevin T McDonnell, and Hong Qin. 2004. Surface reconstruction of noisy and defective data sets. In IEEE visualization 2004. IEEE, 259-266.
- Rui Xu, Zixiong Wang, Zhiyang Dou, Chen Zong, Shiqing Xin, Mingyan Jiang, Tao Ju, and Changhe Tu. 2022. RFEPS: Reconstructing Feature-Line Equipped Polygonal Surface. ACM Trans. on Graphics (Proc. SIGGRAPH Asia) 41, 6 (2022), 1-15.

- $\label{thm:lem:mincheol} \mbox{Mincheol Yoon, Yunjin Lee, Seungyong Lee, Ioannis Ivrissimtzis, and Hans-Peter Seidel.}$ 2007. Surface and normal ensembles for surface reconstruction. Computer-Aided Design 39, 5 (2007), 408-420.
- Brayan S Zapata-Impata, Pablo Gil, Jorge Pomares, and Fernando Torres. 2019. Fast geometry-based computation of grasping points on three-dimensional point clouds. International Journal of Advanced Robotic Systems 16, 1 (2019), 1729881419831846.
- Jie Zhang, Junjie Cao, Xiuping Liu, He Chen, Bo Li, and Ligang Liu. 2018. Multi-normal estimation via pair consistency voting. IEEE Trans. on Vis. and Comp. Graphics 25, 4 (2018), 1693-1706.
- Jie Zhang, Junjie Cao, Xiuping Liu, Jun Wang, Jian Liu, and Xiquan Shi. 2013. Point cloud normal estimation via low-rank subspace clustering. Computers & Graphics
- Jun Zhou, Hua Huang, Bin Liu, and Xiuping Liu. 2020. Normal estimation for 3d point clouds via local plane constraint and multi-scale selection. Computer-Aided Design 129 (2020), 102916.
- Runsong Zhu, Yuan Liu, Zhen Dong, Yuan Wang, Tengping Jiang, Wenping Wang, and Bisheng Yang. 2021. AdaFit: Rethinking Learning-based Normal Estimation on Point Clouds. In IEEE ICCV. 6118-6127.